

**WegCenter/UniGraz Technical Report for EU/GJU No. 1/2006**  
[Doc.No. GAD-RP-003-UG]

EU/GJU study:

**GADEM – Galileo Atmospheric Data Enhancement Mission**

[Contract No: GJU/06/2423/CTR/GADEM – March 2006]

[WP2100: Signal Characteristics & Performance Analysis]

Supported by ESA Prodex Arrangement No. 90152-CN1 (Advanced Topics in RO Modelling and Retrieval)

**End-to-end Scientific Performance Analysis for Retrieval  
of Atmospheric Data from Galileo K-band Radio Links**

M. Schwärz, J. Ramsauer, and G. Kirchengast

Wegener Center for Climate and Global Change (WegCenter),  
University of Graz, Graz, Austria

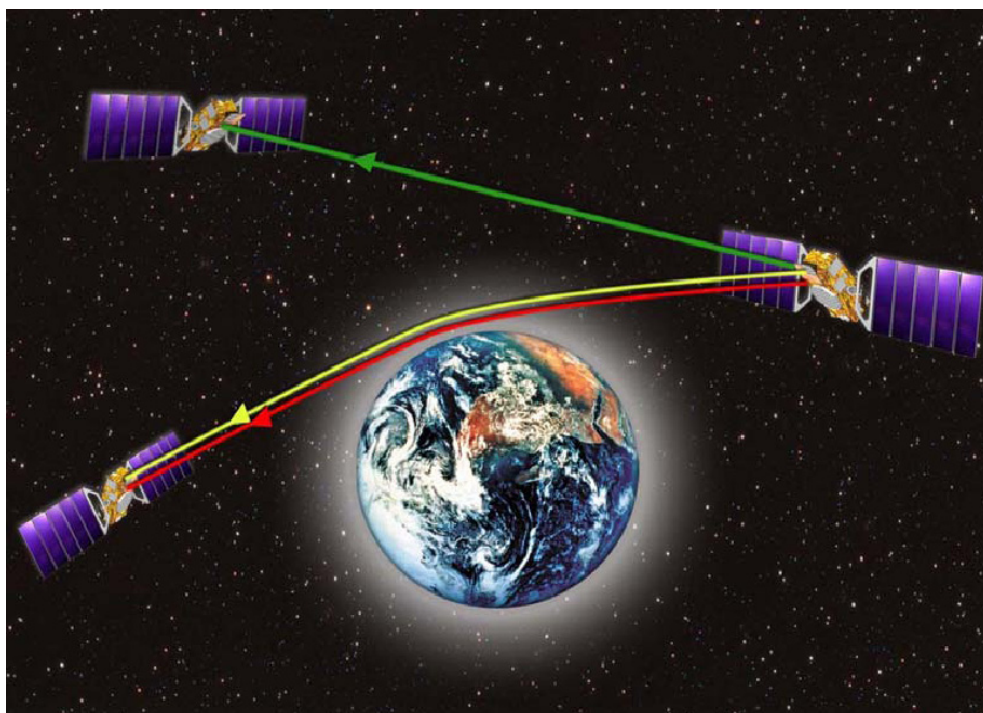


(fig source: GADEM Proposal, Kayser-Threde et al., 2004)

Final version — November 2006

(intentionally left blank; back page if double-sided print)

## Table of Contents

<b>1 INTRODUCTION .....</b>	<b>1</b>
<b>1.1 Study Objectives and Overview.....</b>	<b>1</b>
<b>1.2 Report Overview .....</b>	<b>1</b>
<b>2 STUDY DESIGN AND SIMULATION SETUP .....</b>	<b>3</b>
<b>2.1 Coverage Simulations and Selection of Observation Ensembles.....</b>	<b>3</b>
2.1.1 Galileo-LEO Radio Occultation.....	3
2.1.2 Galileo-GS Radio Links .....	5
<b>2.2 Forward Modeling .....</b>	<b>6</b>
2.2.1 Galileo-LEO K-band Occultation Signal Propagation Modeling .....	7
2.2.2 Propagation Modeling for Galileo-GS K-band Signals .....	8
<b>2.3 Signal Characteristics and Instrumental Error Simulations.....</b>	<b>8</b>
2.3.1 Radio Occultation Signal and Receiving System Simulations.....	8
2.3.2 Galileo-GS Radio Link Signal and Receiving System Simulations.....	11
<b>2.4 Retrieval of Atmospheric Data Products.....</b>	<b>13</b>
2.4.1 K-band Radio Occultation Atmospheric Profiles Retrieval.....	13
2.4.2 Atmospheric Time Series Retrieval for Galileo-GS K-band Links.....	19
<b>3 PERFORMANCE ANALYSIS RESULTS .....</b>	<b>21</b>
<b>3.1 Results for the Galileo-LEO K-band Occultation System .....</b>	<b>21</b>
<b>3.2 Results for the Galileo-GS System .....</b>	<b>31</b>
<b>4 CONCLUSIONS AND OUTLOOK .....</b>	<b>39</b>
<b>REFERENCES .....</b>	<b>41</b>
<b>APPENDIX A: .....</b>	<b>43</b>
<b>A.1. Galileo Constellation Two Line Element (TLE) Files .....</b>	<b>43</b>
<b>A.2. METOP Constellation Two Line Element (TLE) Files .....</b>	<b>44</b>
<b>A.3. Ground Station Properties .....</b>	<b>44</b>
<b>A.4. Mission Analysis/Planning input (example) .....</b>	<b>45</b>
<b>A.5. Forward Modeling input (example) .....</b>	<b>46</b>
<b>A.6. Observation System Modeling input (example) .....</b>	<b>47</b>
<b>A.7. Inversion/Retrieval input (example) .....</b>	<b>49</b>

(intentionally left blank; back page if double-sided print)

## List of Acronyms

ACE+	Atmosphere and Climate Explorer (occultation mission concept studied by ESA 2002–2004)
ECMWF	European Centre for Medium-Range Weather Forecasts
EGOPS	End-to-end GNSS Occultation Performance Simulator
ESA	European Space Agency ( <a href="http://www.esa.int">www.esa.int</a> )
GADEM	Galileo Atmospheric Data Enhancement Mission (Kayser-Threde et al. GJU project)
Galileo	Currently developed European GNSS component (operational ~2009/10)
GNSS	Global Navigation Satellite System(s) (generic term)
RO	radio occultation
GS	Ground Station (typically Galileo ground station in the context of Galileo-to-GS links)
IWV	Integrated Water Vapor [ $\text{kg/m}^2$ ] (from Galileo-to-GS links; slant IWV or vertical IWV)
K band	link signals within 17–23 GHz
L band	link signals within 1–2 GHz
LEO	Low Earth Orbit (or satellite in Low Earth Orbit)
MPM	Millimeter-wave Propagation Model
MRD	Mission Requirements Document
POD	Precise Orbit Data
PW	Precipitable Water [mm] (from Galileo-to-GS links; derived from vertical IWV data)
SIWV	Slant Integrated Water Vapor [ $\text{kg/m}^2$ ] (cf. IWV)
SNR	Signal-to-Noise Ratio (typically of the received signals, in the context of this Tech. Note)
TLE	two line element
Tx, Rx	Transmitter (Tx) resp. Receiver (Rx); also Transmitter resp. Receiver satellite
UT	Universal Time

(intentionally left blank; back page if double-sided print)

## 1 Introduction

The present report deals with Work Package 2100 (WP 2100) of the Galileo Atmospheric Data Enhancement Mission (GADEM) study on the proposed novel K-band links. The K-band links are designed to be a complementary investigation method to the well known L-band links (e.g., Melbourne et al., 1994; Hoeg et al., 1995; Kursinski et al., 1997; Steiner et al., 2001; Lee et al., 2001). WP 2100 is intended to provide a signal characterization for the proposed system as well as a performance analysis for the retrieved atmospheric data products, like temperature and humidity profiles (in the case of satellite-to-satellite measurements) or integrated column amounts of humidity (in the case of satellite-to-ground measurements).

### 1.1 Study Objectives and Overview

The overall objective of this study is the characterization of the retrieval performance for a typical set of instrumental errors by atmospheric sounding using the proposed GADEM K-band link scenario. For this set of instrumental errors a statistical performance analysis using geometric optics processing (GOP) is carried out for realistic atmospheric conditions using high resolution ECMWF analysis fields including liquid water and ice water clouds. Additionally, the atmospheric conditions comprise meaningful turbulent conditions.

In particular, the present performance analysis deals with the investigation of GNSS-LEO and GNSS-to-ground station (GS) measurements. GNSS-GNSS (Galileo-Galileo) links were not examined in this report, since the constellation analysis (Kayser-Threde, 2006a) yielded that they are not distributed globally (a requirement in WegCenter/UniGraz (2006)) but mainly clustered in two narrow latitudinal bands near the high-latitude turning points of the Galileo satellite sub-orbital tracks. The study will present the differences in performance using the main GADEM setup, i.e., using the two main GADEM frequencies only (17.25 GHz and 22.6 GHz), and utilizing all three frequencies including the optional 20.2 GHz. In the case of GNSS-GS measurements we focus on the differences in performance between a phase-based retrieval, which can also be carried out when using L-band frequencies and the K-band based amplitude retrieval. Additionally, the gain in performance when combining both methods is presented.

### 1.2 Report Overview

The report is structured as follows: In section 2, the performance simulation setup used for the study is presented. In particular, a description of the simulation tool EGOPS5 and a detailed description of the retrieval algorithms are provided in this section. Section 3 summarizes all analysis results and shows statistical profile retrieval performance results. The focus of the GNSS-LEO part lies on the temperature and humidity results, in the case of GNSS-GS measurements the slant integrated water vapor (SIWV) is inspected in detail. In section 4, a brief summary and conclusions are given.

(intentionally left blank; back page if double-sided print)



## 2 Study Design and Simulation Setup

The present study contains two parts as scheduled in the GADEM Proposal. There are the simulations of the Galileo-LEO radio occultations on the one hand and the Galileo-GS measurements on the other hand. The simulations were mainly performed with EGOPS5.2, the newest version of the EGOPS software system, which has been developed from EGOPS5.0 and EGOPS4 and is an extension and advancement of them. In contrast to EGOPS4 (Kirchengast 1998; Kirchengast et al., 2002), EGOPS5.0 also allows K-band occultation simulations and is now – in version 5.2 – amongst other things extended to GNSS-GS K-band signal processing. The retrieval of the GNSS-GS simulations is the only thing, which was performed off-line since this is currently not a part of the EGOPS system.

### 2.1 Coverage Simulations and Selection of Observation Ensembles

#### 2.1.1 Galileo-LEO Radio Occultation

The events used in the Galileo-LEO simulations were selected by assuming a set of 27 Galileo satellites exhibiting a standard orbit constellation as transmitting systems and a METOP like LEO as receiving system (sun synchronous orbit with an inclination of about  $98^\circ$  and a height of about 830 km). The corresponding orbital elements are listed in Appendix A.1 in the form of “Two Line Element” (TLE) sets. The nominal start time was set to July, 1, 2009, 0 UT.

In Figure 1 the coverage by occultation events for six individual days over a period of three months, is illustrated. The typical daily coverage exhibits about 600 to 670 events per day. A detailed view shows an increasing number of events for this period due to the orbit shift of the Galileo satellites. Figure 2 shows the monthly coverage for July 2009 for the used constellation. It is illustrated that the earth is evenly scanned by about 19.000 events per month. Only the tropical region exhibits a thinner coverage as a result of an inclination of about  $56^\circ$ .

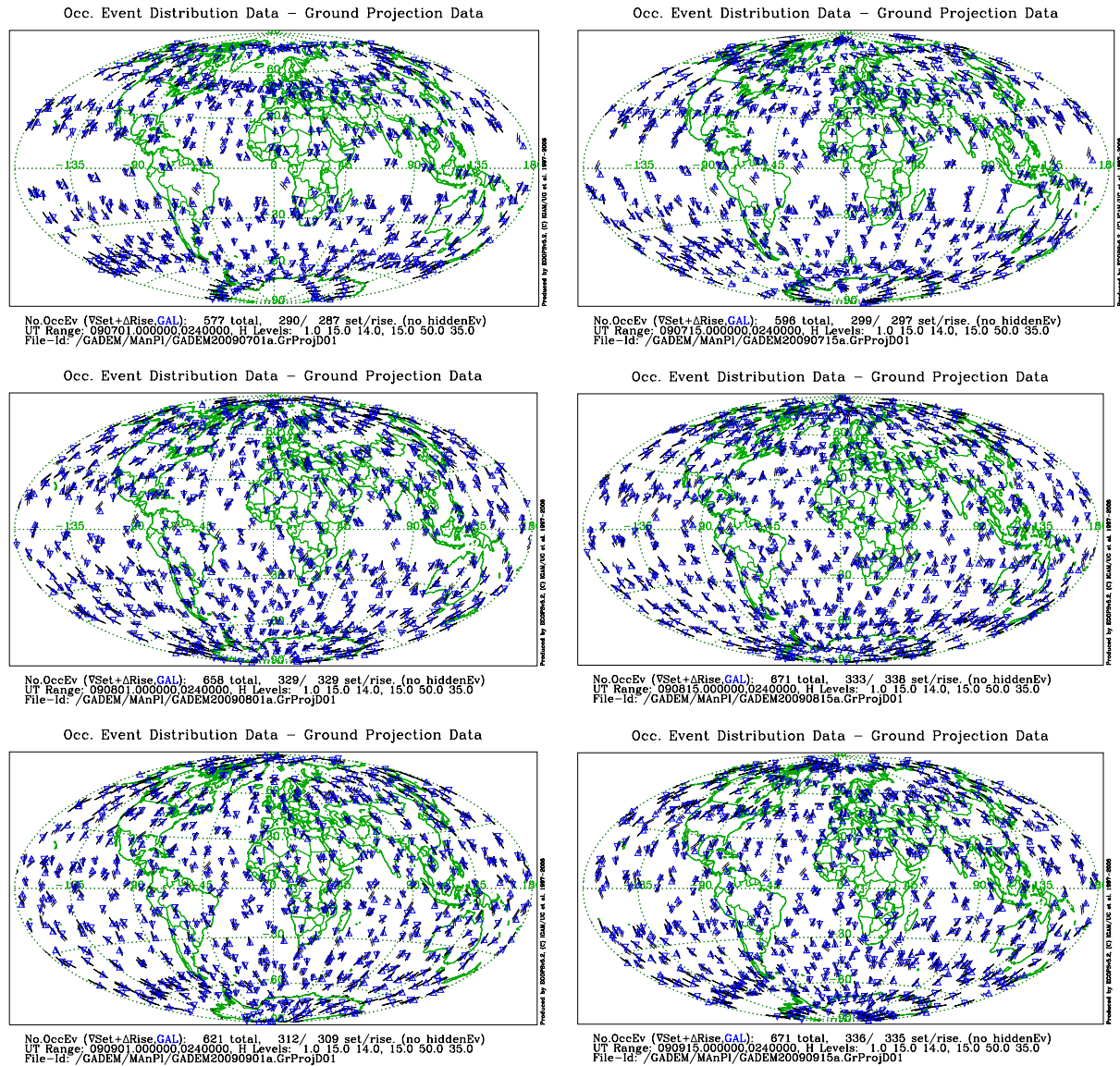


**Fig 1.** Coverage by Galileo-LEO occultation events for individual days over three months, illustrating the typical daily coverage by about 600 to 670 events per day. Shown are the simulation results for 1 Jul 2009 (upper left), 15 Jul 2009 (upper right), 1 Aug 2009 (middle left), 15 Aug 2009 (middle right), 1 Sep 2009 (lower left), 15 Sep 2009 (lower right).

The time range used for the simulations was 24 hours starting at July 1, 2009, 00:00 UT, as mentioned above. To account for possible dependencies on the latitudinal distribution of the events they were divided into three different regions – a tropical zone ( $-20^{\circ}$  to  $20^{\circ}$  latitude), an extratropical northern hemisphere ( $30^{\circ}$  to  $90^{\circ}$  latitude), and an extratropical southern hemisphere ( $-30^{\circ}$  to  $-90^{\circ}$  latitude) zone. The samples obtained by this classification were then arbitrarily down-selected to about 60 events per zone which were subjected to the forward modeling and data inversion process.

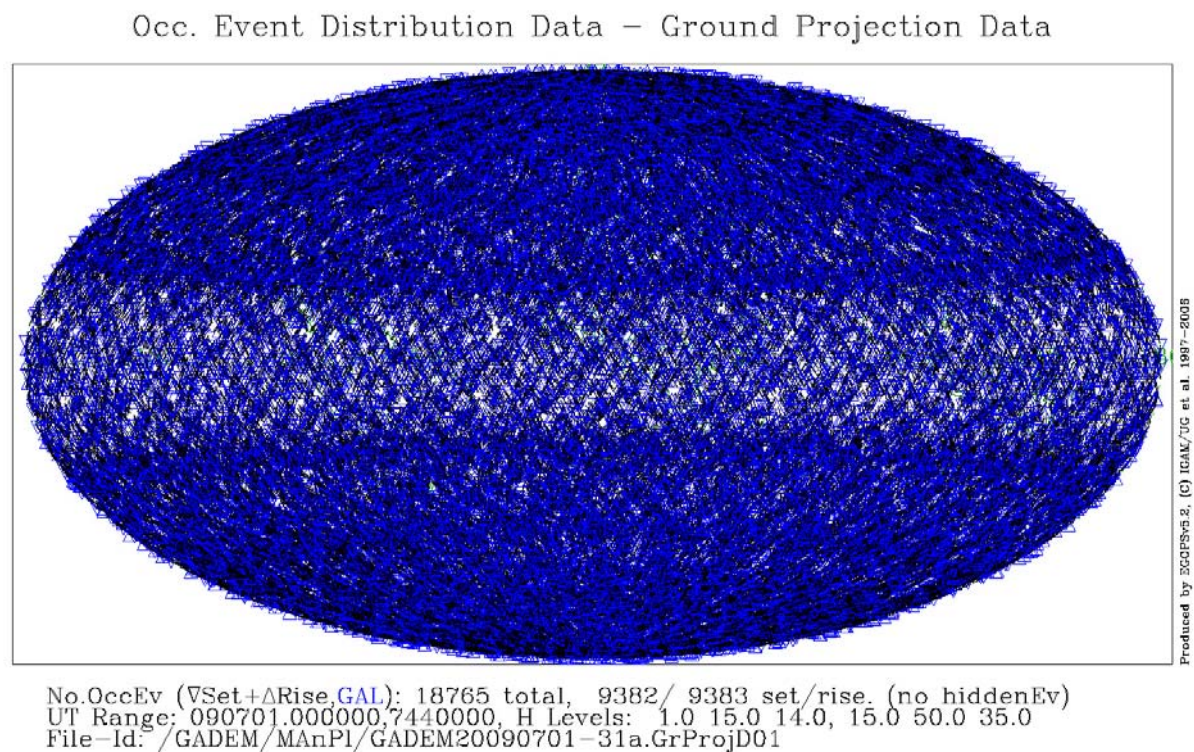


**Fig 2.** Coverage by Galileo-LEO occultation events over a full month, illustrating the typical monthly coverage by about 19,000 events per month. Shown are the simulation results for July 2009.

### 2.1.2 Galileo-GS Radio Links

In the case of the Galileo-GS radio link measurements 10 stations (c.f. Figure 3, left panel) were selected arbitrarily but with the intention to distribute them evenly on the globe to serve as receiving systems. These stations were then subjected to a visibility analysis performed with the EGOPS software system. The transmitting system used in the visibility study was assumed to have the same constellation as in the case of the Galileo-LEO occultations. The Galileo satellites were assumed to be visible if they are at least  $15^\circ$  above the horizon.

The nominal observational time range was set to three hours. For each of the 10 stations 4 GNSS-GS events were selected out of the obtained sample. The only constraint for the selection was that the transmitting satellite is visible by the ground station at least 90 minutes. As an example of such an event Figure 3, right panel, shows a fan received by the ground station at Maspalomas (Canaries) and spanned by a Galileo Satellite.

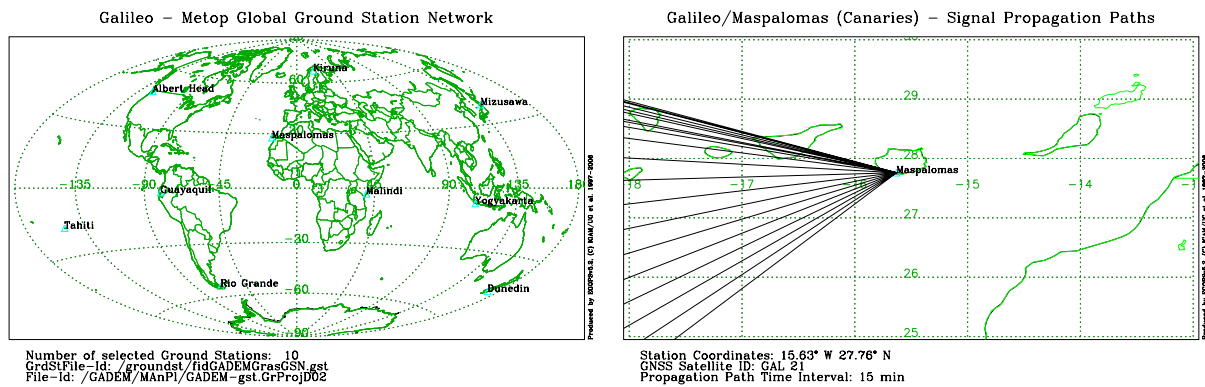


**Fig 3.** Geographic distribution of the ten selected representative Galileo ground stations (GS) used for the simulation of Galileo-GS radio links (left panel) and enlarged view to one GS (Maspalomas), illustrating radio links to one Galileo satellite in 15-min time steps (right panel).

## 2.2 Forward Modeling

Forward Modeling and the subsequent Observation System Modeling in EGOPS are the basis for providing reasonably realistic simulated observables of phase and amplitude profiles at all relevant frequencies. K-band forward modeling in EGOPS5 consists of three main elements: the orbit arcs simulations which finds the orbit sections of the transmitter (Tx) and receiver (Rx) orbits necessary for performing the forward modeling (ray-by-ray from Tx to Rx over the full occultation event, if using a ray tracer), the transmitter signal simulations and the signal propagation simulations, which also involve simulation of the atmosphere/ionosphere environment. The simulation conditions are based on user-specified input parameters like type of occultation event, atmospheric and ionospheric model and conditions, sampling rate, type of propagation simulator, etc. An example of such a forward modeling input file is shown in Appendix A.3.

**Orbit arcs computations**, which can be done using “ideal” or “realistic” geometry, create the so called **simulated geometry data**. This data contains the satellite positions [km] and velocities [km/s] along the orbit arcs of the specified transmitter and receiver satellites, respectively, at the specified sampling rate for the current occultation event. It is required as a geometric baseline for the subsequent signal propagation simulations. As a convenient sideline, also “true” tangent point profile estimates from ray-tracers are stored with these data.

The **transmitter signal simulations** determine the carrier-frequencies and transmitted powers of the occultation signals. The GADEM Tx set contains the three nominal frequencies with values of  $F1 = 17.25$  GHz, ( $F2 = 20.2$  GHz, optional) and  $F3 = 22.6$  GHz. The corresponding transmitter signal powers amount to ~14-16 dBW for each frequency.

The **signal propagation simulations** can be carried out using the “full-3D ray tracer” (which fully accounts for the three-dimensional refractivity field and its first two derivatives), the “quasi-3D ray tracer” (which, besides the field, only accounts for vertical refractivity gradients and curvature) or the “wave optics propagator”. Currently (EGOPS5.2 status) and for this study, the full-3D ray tracer is the only tool to be used. The tools create the **simulated signal data**, which include the main observables excess phase [m] and atmospheric loss [dB] for each frequency at the specified sampling rates for the occultation event in consideration.



Subsequently, this data is used as input data within observation system and inversion/retrieval processing. In addition, “true” bending angles [mrad] and “true” transmissions (due to absorption only) [dB] are computed as extended output, and the data also include “true” Doppler shifts [Hz] and “true” impact parameters [km] for each frequency. In the case of GNSS-GS simulations the “true” slant integrated water vapor (SIWV) [kg/m<sup>2</sup>] is also part of the output.

Rigorous modeling of atmospheric absorption loss is a new feature introduced in EGOPS5. Total atmospheric loss now consists of atmospheric loss due to defocusing and atmospheric loss due to absorption, which are considered separately. The geometric-optics computation is done in this way: For each sample in an occultation, the ray that goes from a specified transmitter position to a specified receiver position is found via precision ray-tracing. The tracking of the receiver is done with a few trials of ray paths, using Newton-Raphson's method of finding roots. After calculating initial ray parameters in degrees and total phase [km], the ray path is calculated by solving Haselgrove's three-dimensional differential equations (six equations) and the relative flux density is measured by solving twelve additional equations (Syndergaard, 1998). The eighteen equations in total are solved by numerical integration using a Runge-Kutta method and a predictor-corrector method especially designed to deal with adaptive stepsize. During the integration, in addition to the ray path calculation, the defocusing loss of the signal power is computed. After the refracted ray path is precisely known this way, along ray computation of absorption loss is done using the Bouguer-Lambert-Beer law (neglecting emission as we have strong source intensity in active limb sounding),

$$I = I_0 \cdot e^{-\int_{l_0}^{l_1} \kappa(l) dl} = e^{-\tau},$$

where  $I$  is the received signal intensity,  $l$  the coordinate along the ray path,  $l_0$  the point of the considered part of the ray path farthest away from the sensor (to be placed above the atmosphere at ~80 km height so that beyond absorption is essentially negligible),  $l_1$  the sensor-closest point of the ray path (also at ~80 km),  $I_0$  the un-attenuated intensity at  $l_0$ ,  $\kappa$  the absorption coefficient along the ray path, which is proportional to imaginary refractivity, and  $\tau$  the optical thickness (extinction coefficient, in general, but scattering is negligible in the present context). The absorption coefficient  $\kappa$  is calculated point-by-point along each ray for the given atmospheric conditions invoking the MPM93 (e.g., Liebe et al., 1993) imaginary refractivity model based on a selected atmospheric model (supplying temperature, water vapor, clouds,...). Using Simpson's integration rule, total optical thickness  $\tau$ , and transmission ( $I/I_0$ ) resp. absorption loss ( $I_0/I$ ), are then calculated at the receiver end of the ray and added to the defocusing loss.

## 2.2.1 Galileo-LEO K-band Occultation Signal Propagation Modeling

In the case of Galileo-LEO K-band occultation signal propagation, perturbations by an atmospheric turbulence/scintillation model are superposed onto the total atmospheric loss. For further information see Kuhn (2003).

All forward modeled events made for this study were simulated using high-precision 3D ray tracing with sub-millimetric accuracy and a sampling rate of 10 Hz. The underlying

atmosphere was a high resolution ECMWF analysis field (12 UT analysis of March. 15, 2006; near-equinox date, otherwise arbitrarily chosen).

## 2.2.2 Propagation Modeling for Galileo-GS K-band Signals

In the case of Galileo-GS K-band signal propagation modeling a sampling rate of 0.1 Hz was used. Since the orography used in the ECMWF model disagrees with the orography of the real world, the height of the observing ground station has to be raised (or dropped) to the model height to address the special properties of the model.

## 2.3 Signal Characteristics and Instrumental Error Simulations

Reasonably realistic modeling of the main K-band instrumental errors has been performed, including thermal amplitude noise and linear amplitude drifts, e.g., due to slight antenna gain drift. For setting the error modeling input values, we followed the specifications as laid out in WegCenter/UniGraz (2006) and Kayser-Threde (2006b). As an example, an EGOPS “Observation System Modeling” input specification file is listed in Appendix A.4, which has all error models illustrated below enabled with the input settings used.

In this context also a realistic link budget is needed in order to have a reasonable carrier-to-noise density ratio ( $C/N_0$ ) input to the noise modeling.

### 2.3.1 Radio Occultation Signal and Receiving System Simulations

This link budget derives in EGOPS5 “automatically” from the end-to-end simulation of all link budget components from transmitter power (set to ~14-16 dBW) via transmitter antenna gain (30 dB), space loss, and receiver antennae gain (~25-28 dB) to received amplitude (for more detailed information, see the mission requirement specifications in Kayser-Threde (2006b)). Figure 4 illustrates  $C/N_0$  profiles for an example case. With the settings used in this study, a  $C/N_0$  figure of ~66 dBHz at 25 km height (or ~67 dBHz in “vacuum” above the atmosphere) is found. Based on the results shown in section 3, this is evidently a quite adequate figure to size the GADEM link budget for achieving the observational requirements.

In order to illustrate the characteristics of the different error sources mentioned above, they are illustrated in Figures 5 to 7 below.

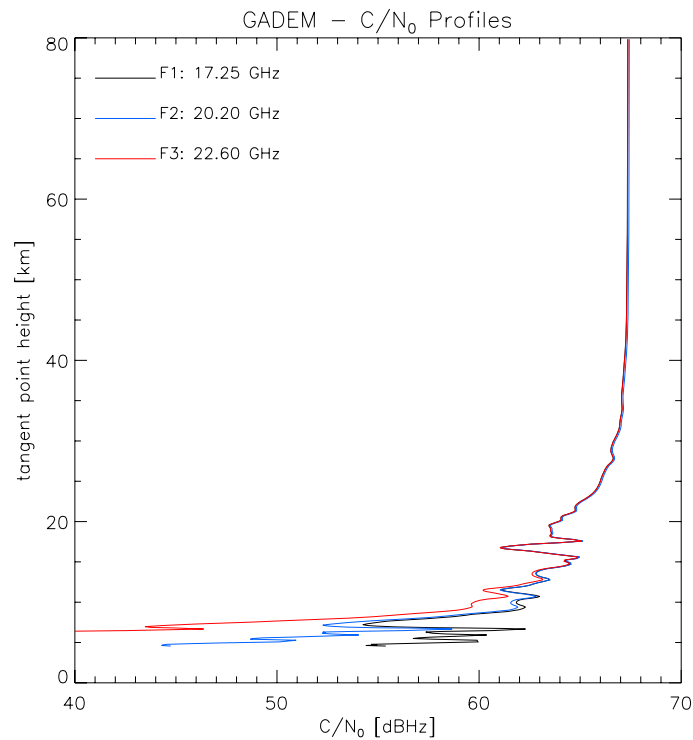


**Fig 4.** Carrier-to-noise density ratio (C/N<sub>0</sub>) profiles for the two (F1, F3) resp. three (F1, F2, F3) GADEM frequencies for an arbitrary profile modeled from an ECMWF analysis field.

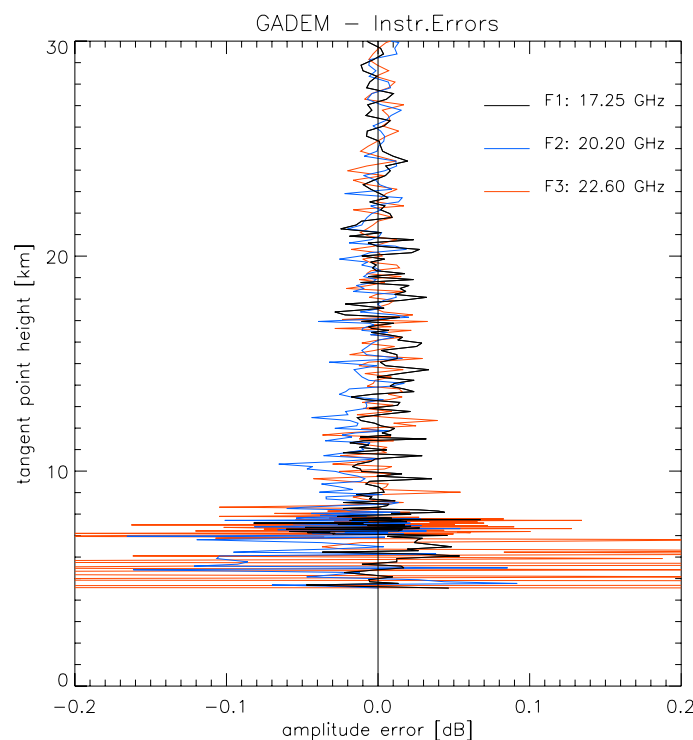


**Fig 5.** Exemplary realizations of total instrumental error profiles for the two (F1, F3) resp. three (F1, F2, F3) GADEM frequencies. Both error sources illustrated below in Fig. 6 and Fig. 7 are included with model settings as noted in the below captions.

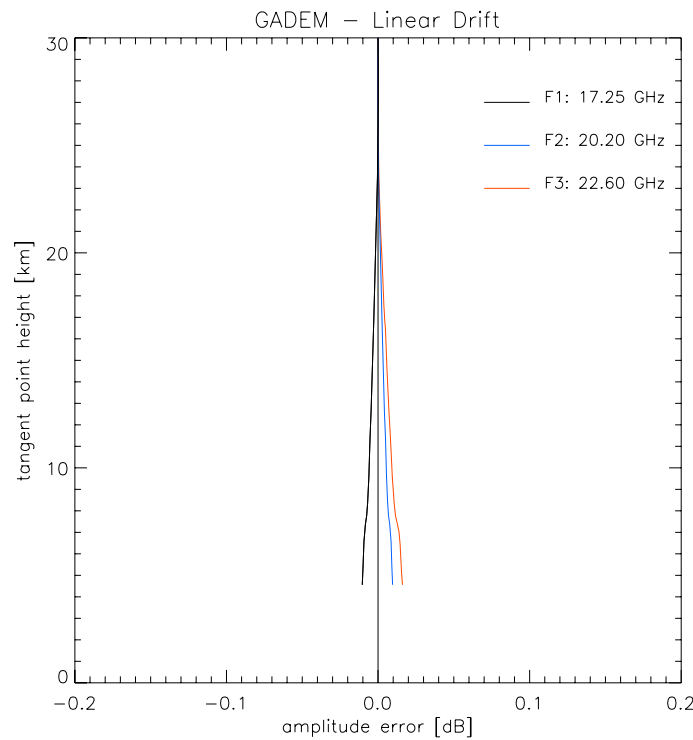


**Fig 6.** Exemplary realizations of linear amplitude drift profiles for the two (F1, F3) resp. three (F1, F2, F3) GADEM frequencies. The main amplitude drift model setting was a linear drift slope of 0.06 dB/min, with the drift starting at the occultation event time corresponding to a tangent height of 25 km.

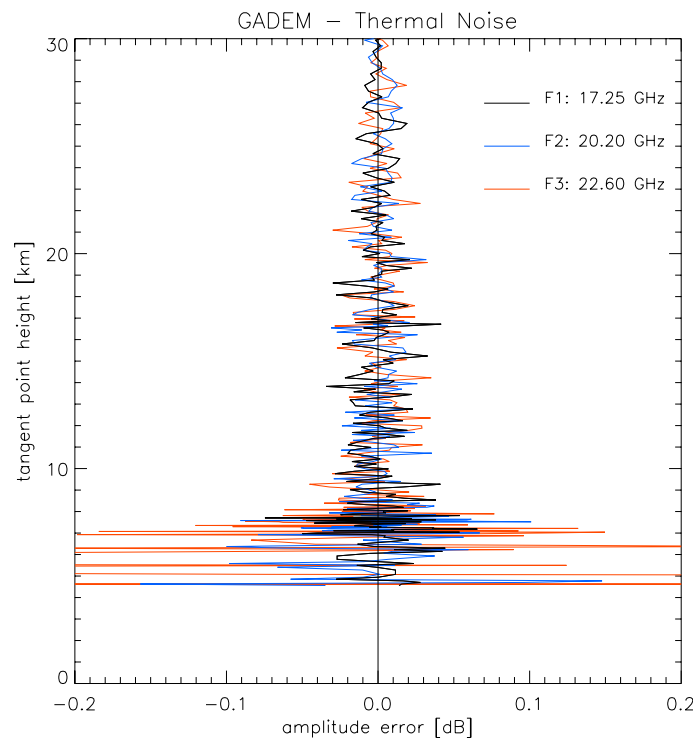


**Fig 7.** Exemplary realizations of thermal amplitude noise profiles for the two (F1, F3) resp. three (F1, F2, F3) GADEM frequencies. The downward increase of thermal noise with the gradual  $C/N_0$  decrease (Fig. 4) is well visible. The main thermal noise model settings were 80 K antenna noise temperature and 160 K receiver noise temperature.



### 2.3.2 Galileo-GS Radio Link Signal and Receiving System Simulations

The link budget for the Galileo-GS signal simulations consists of  $\sim 4.4$ - $10.8$  dBW (transmitter power), 12 dB (transmitter antenna gain), space loss, and  $\sim 34$ - $36$  dB (receiver antennae gain). Figure 8 illustrates  $C/N_0$  time series for an example case. With the settings used in this study, a  $C/N_0$  figure of  $\sim 50$  dBHz at nadir (or  $\sim 49$  dBHz, near horizontal view) is found. In section 3 it is shown that this is evidently a quite adequate setup to size the GADEM link budget for achieving the observational requirements.

For the phase-based GNSS-GS retrieval (which can also be applied to the original Galileo L band frequencies without needing the GADEM K-band channels) an overall Gaussian noise of 5 mm/min was added to account for several errors, which can occur (value taken from experience with L band systems, e.g., Foelsche and Kirchengast (2001); and references therein). Additionally, a linear phase drift slope of 1 (or 3) mm/min was added to test the dependency of the retrieval performance on such drifts.

In order to illustrate the characteristics of the different error sources relating the amplitude retrieval mentioned above, they are illustrated in Figures 9 and 10 below.

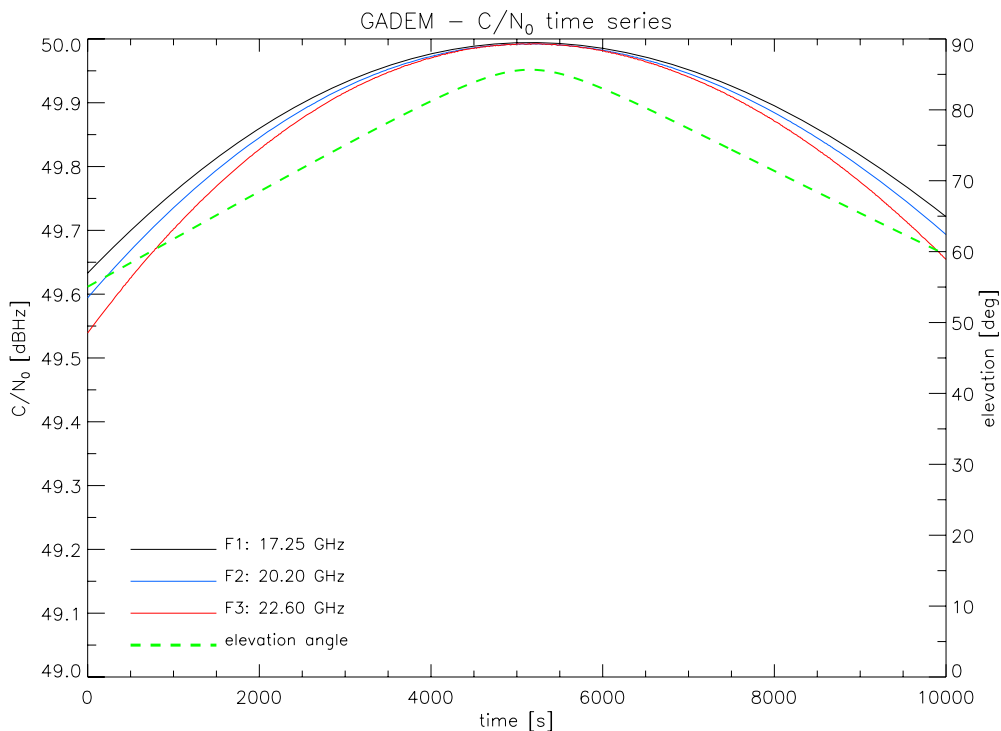


**Fig 8.** Carrier-to-noise density ratio ( $C/N_0$ ) time series for the two (F1, F3) resp. three (F1, F2, F3) GADEM frequencies for an arbitrary GNSS-GS measurement sequence of several hours duration, modeled from an ECMWF analysis field.

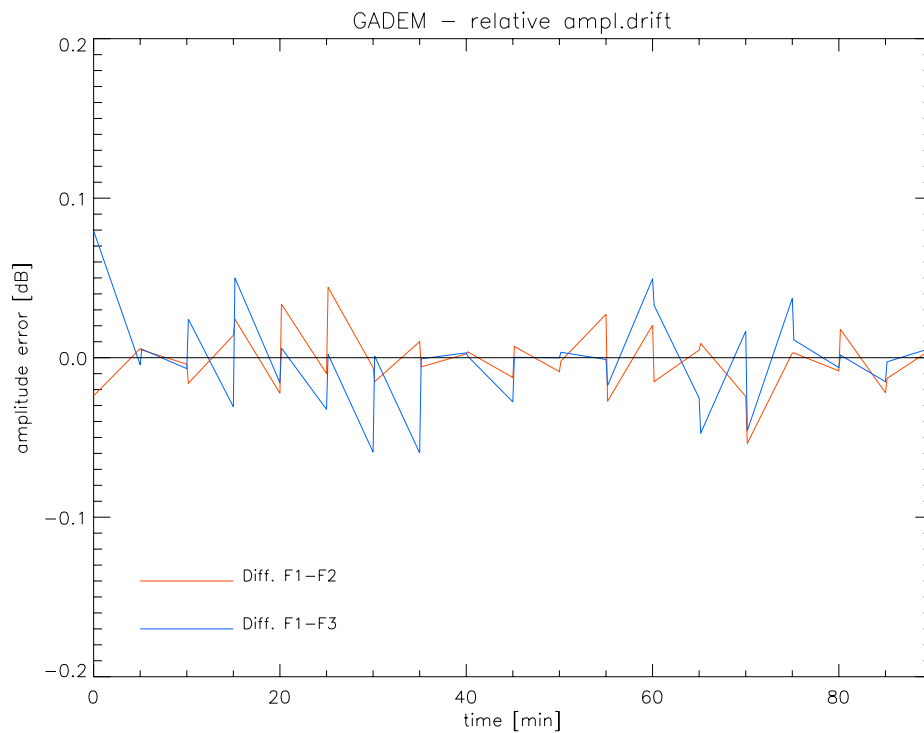


**Fig 9.** Exemplary realizations of linear amplitude drift time series plotted here as differential drifts between F1–F2 and F1–F3, respectively. The main amplitude drift model setting was a linear drift slope of 0.02 dB/min on the differential amplitude (in units [dB]), with a duration of 5 min (one measurement sample) starting randomly between -0.1 and 0.1 dB (random distribution of slopes).

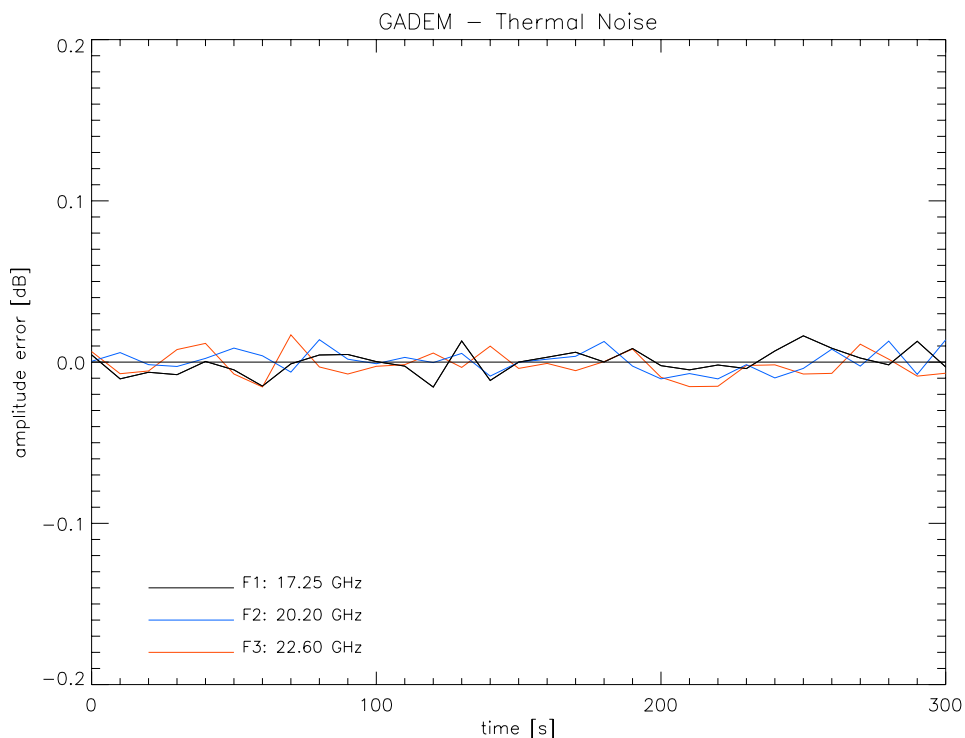


**Fig 10.** Exemplary realizations of thermal amplitude noise time series for the two (F1, F3) resp. three (F1, F2, F3) GADEM frequencies, for one individual 5-min sample (sampled at 0.1 Hz rate). The main thermal noise model settings were 80 K antenna noise temperature and 160 K receiver noise temperature.

## 2.4 Retrieval of Atmospheric Data Products

### 2.4.1 K-band Radio Occultation Atmospheric Profiles Retrieval

The scientific processing of K-band occultation data starts from phase and amplitude data, supplemented by the necessary geometric information, and proceeds via Doppler shifts, bending angles, and transmissions down to quasi-vertical atmospheric profiles of real and imaginary refractivities, density, pressure, geopotential height, temperature, humidity, and liquid water. The algorithms consist of the following main steps:

1. bending angle and transmission retrieval,
2. real and imaginary refractivities retrieval,
3. atmospheric profiles retrieval.

Bending angle and transmission retrieval as well as refractivities retrieval proceed similarly to the L-band case and will be only briefly addressed below. The emphasis is placed on the atmospheric profiles retrieval, where a description of a robust optimal estimation processing scheme is given. More details on the algorithms can be found in Kirchengast et al. (2004a) and Nielsen et al. (2003), with complementary information also, e.g., in Kursinski et al. (2002) and Kursinski et al. (2004).

The general processing concept is illustrated in Figure 11, and the related general procedure is as follows (details on each of the five steps are given below).

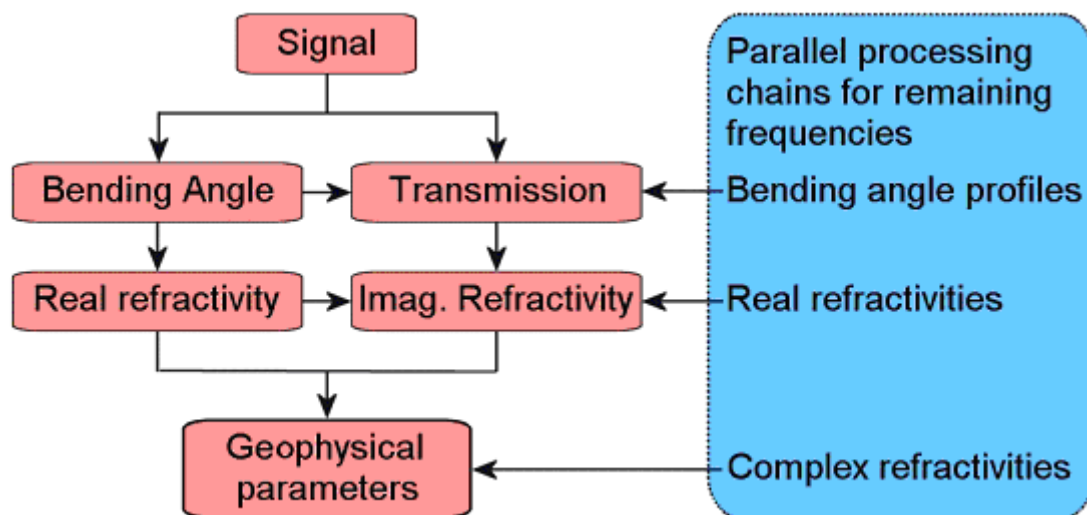


**Fig 11.** K- band retrieval processing chain overview. The five upper boxes to the left represent the processing chain for a single frequency channel, whereas the box to the right represents parallel processing chains for the remaining carrier frequencies in the system. (after Nielsen et al., 2003).

The processing chain was implemented as part of the End-to-end Generic Occultation Performance Simulator, version 5 (EGOPS5), which was developed in course of the ESA-

ACEPASS (ACE+ Phase A Scientific Support, cf. Kirchengast et al., 2004a) study on K-band characterization, based on heritage from the L-band simulator EGOPS4 (Kirchengast et al., 2002).

## ***Bending Angle and Transmission Retrieval***

The phase and amplitude profiles are used together with the corresponding POD data comprising positions and velocities of LEO transmitter and LEO receiver satellites to determine the atmospheric bending angle profile as a function of impact parameter in the same way as in the well-known L-band processing. If wave-optics processing is utilized, both phase path changes (Doppler shift profiles) and normalized amplitude profiles (raw transmission profiles) are used in this process, whereas if geometric-optics processing is performed only Doppler shift profiles are used.

The amplitude profiles at each K-band signal frequency (GADEM nominal frequencies near 17.25 GHz, 20.2 GHz, 22.6 GHz), the impact parameter profile, and the transmitter and receiver position profiles are used to compute the transmission profiles due to atmospheric absorption at each frequency. The exact way to subtract amplitude defocusing and spreading from the measured amplitude profiles, in order to obtain the transmission profiles due to absorption only, depends on whether wave-optics or geometric-optics processing is utilized.

In case differential transmission retrieval is performed, an option used in this study, the direct transmissions derived at the individual frequencies are combined into difference-pairs. That is in case of the GADEM two-frequency system (F1 and F3) one differential transmission profile is then available (F3–F1), in case of the optional three-frequency system (F1, F2, F3) it is two differential transmission profiles (F2–F1, F3–F2). The subsequent processing towards imaginary refractivities (absorption coefficients) and atmospheric profiles is formally identical for both direct-transmissions and differential transmissions. It is just that in the latter case the further steps start with the differential profiles (which is one profile less) instead of the direct profiles. The reason for using differential transmissions as an alternative is that in case of significant atmospheric turbulence this retrieval mode is significantly more robust and accurate. In practice one would thus use either direct or differential transmissions dependent on the indications of the level of atmospheric turbulence for a given occultation event.

A key step in transmission retrieval is the normalization to a reference height “above the absorptive atmosphere”, where the transmission is unity (~25 km in the GADEM case). This is the step where the intrinsic self-calibration of the amplitudes comes in: similar to the self-calibrated bending angles, this normalization implies that as long as the transmission measurements are short-term stable over the ~30 sec of the occultation event from about 25 km towards the surface, each individual profile is a self-standing reliable measure of the atmospheric absorption at the given place and time, independent of any other measurements. Moreover, since the absorption coefficient (or imaginary refractivity) obtained from the transmission depends on the impact parameter-derivative of transmission only, a small constant transmission residual does not matter.

## ***Real and Imaginary Refractivities Retrieval***

The bending angle profile as a function of the impact parameter is converted to the real refractivity profile as a function of height via the classical L-band Abel transform. Based on this, the real refractivity profile and the impact parameter profile are used together with the transmission profiles at each K-band frequency to derive the absorption coefficient profiles as a function of height with another Abel transform akin to the classical one (same Abelian integration kernel but different in integrand; Kursinski et al., 2002; Kirchengast et al., 2004a). Since imaginary refractivity is proportional to the absorption coefficient, the latter can be obtained alternatively or in addition.

If data assimilation of K-band data products is performed, the refractivity profiles obtained will be the Level 2 data products most conveniently used in such schemes, since both real and imaginary refractivities are, at any point in space and time, just local functions of the atmospheric parameters.

## ***Atmospheric Profiles Retrieval***

The real and imaginary refractivity profiles are associated with four equations: three equations from the frequency dependent imaginary refractivity profiles ( $N_1^I, N_2^I, N_3^I$ ) and one equation from the real part ( $N^R$ ), because this is practically non-dispersive for the considered frequencies. While the equation for the real part is a simple formula (Smith and Weintraub, 1953), the equations behind the imaginary refractivity as a function of the atmospheric parameters are more elaborated and embodied in a Millimeter-wave Propagation Model (MPM) (e.g., Liebe et al., 1993). Together with the hydrostatic equation and the equation of state, there is a set of six equations to derive the four desired atmospheric parameters: pressure, temperature, humidity and liquid water. The latter, cloud liquid water, is retrieved as a by-product since it can have a strong impact on the absorption signal and is an important parameter for both climate science and meteorology.

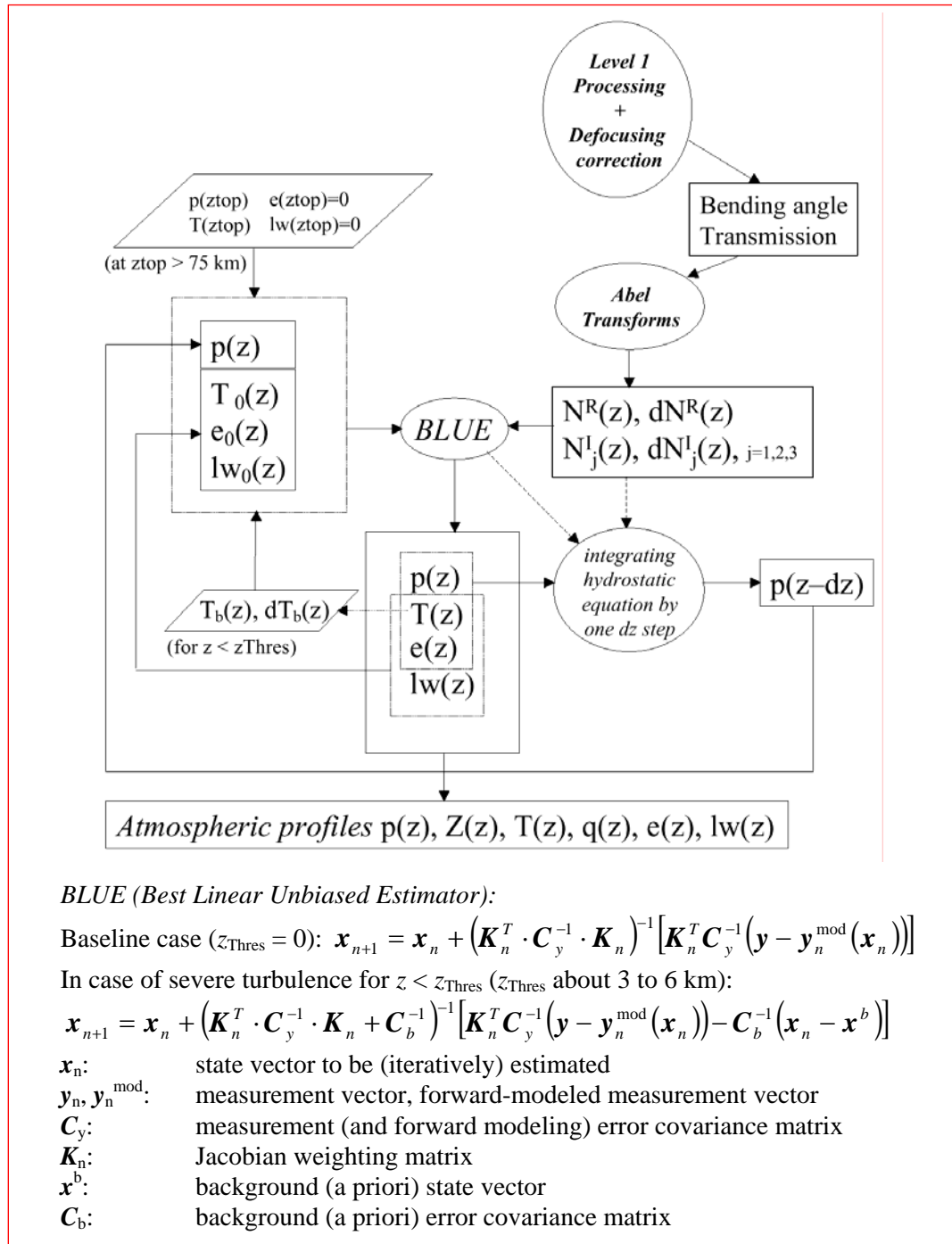


**Fig 12.** Schematic view of the K-band level 2 processing.

Figure 12 schematically illustrates the K-band Level 2 processing with particular emphasis on the atmospheric profiles retrieval. The retrieval begins at a topmost layer and works downward towards the surface at height steps of 100 m or smaller. The problem of retrieving the atmospheric state (pressure  $p$ , temperature  $T$ , water vapor pressure  $e$ , cloud liquid water density  $lw$ ) from the refractivities ( $N^R$ ,  $N^I_1$ ,  $N^I_2$ ,  $N^I_3$ ) is efficiently solved by a downward integration of the hydrostatic equation, to sequentially obtain  $p$ , combined with an iterative Best Linear Unbiased Estimation (BLUE) solution (Rodgers, 2000) at each integration step to

obtain  $(T, e, lw)$  from  $(p, N^R, N_1^I, N_2^I, N_3^I)$ . The BLUE algorithm is initialized by the atmospheric state obtained at the previous height level. The hydrostatic integration provides the pressure “backbone” for this estimation and ensures it to be very robust and reliable. The BLUE requires the specification of covariance matrices for the refractivity data, which are formulated based on the knowledge of their respective error characteristics. The initialization of the whole algorithm is made at high altitudes (e.g., 75 km) with some initial state  $(p_{top}, T_{top}, e_{top}=0, lw_{top}=0)$ , the accuracy of which is non-critical as initialization errors decay quickly over about the first two to three scale heights.

Practically, above a certain height above which water vapor has a negligible effect (~20 km), only  $T$  is estimated. Furthermore, above a certain height above which liquid water is negligible (~8 km), only  $(T, e)$  is estimated. Below, the full state  $(T, e, lw)$  is estimated, which requires at least 3 independent elements of information in  $(p, N^R, N_1^I, N_2^I, N_3^I)$ . Due to the insensitivity to ice clouds  $c$ , no ice water retrieval is needed.

Because the set of equations is somewhat over-determined, it is still possible to retrieve all desired parameters if one of the imaginary refractivity information pieces is lost, as it will be the case at any given height level, where only two of the three frequencies provide amplitude data in useful dynamic range. The information on real refractivity at the lowest of the transmitted frequencies will be lost only in extreme (and rare) situations. If the imaginary refractivity variances grow large enough into the lower troposphere so as to render the BLUE problem effectively underdetermined, which can happen in case of atmospheric turbulence, the advanced processing described below will be used.

### *Processing in case of severe atmospheric turbulence*

Strong amplitude scintillations due to atmospheric turbulence can introduce significant noise into the imaginary refractivity data and may degrade the above baseline retrieval of atmospheric profiles below about 3 to 6 km in the troposphere. However, since the parts of the signal affected by scintillation can be identified thanks to the high sampling rate of the raw measurements (1 kHz), this enables a constant monitoring of the high frequency fluctuations and the determination of a “threshold height”,  $z_{Thres}$ , below which the imaginary refractivity data should be used with caution and potentially receive low to negligible weight in the BLUE process. As turbulence is a layered phenomenon (e.g., Gage, 1990), usually only some fraction of the height levels below  $z_{Thres}$  may need to receive such down-weighting. This will have to be confirmed in future studies. In the performance analyses of section 3 it has been assumed, as a conservative limit, that the complete height range below any  $z_{Thres}$  found is filled with turbulence and is down-weighted.

In case of down-weighting applied to imaginary refractivities below  $z_{Thres}$ , one sensible way to cure the consequent under-determination of the BLUE problem is to introduce weak background (a priori) information into the retrieval at the height levels concerned. The primary candidate information for this purpose is temperature, since it is well predictable in the troposphere above the boundary layer and since it is sufficient auxiliary information under all conditions to ensure a robust estimation. Suitable background temperature profiles ( $T_b$ ) can be obtained from a profile search in an adequate database (e.g., from a 24h ECMWF forecast in a geographic area of some degrees around the profile co-located with the measurement). The  $T_b$  profile selected can be the one that best fits the retrieved temperature profile in the troposphere right above  $z_{Thres}$ , where the retrieved data are still very accurate and allow for a

good fit. The fit to the retrieved data, and not just selection of a co-located profile, is to avoid importing any potential small bias from the background into the retrieval (though ECMWF temperatures below 8 km are essentially unbiased). In producing the performance results for section 3 below, this “best-fit  $T$  extrapolation” approach has been used for heights below  $z_{\text{Thres}}$  and found to ensure accurate humidity and temperature retrieval also under severe turbulence conditions.

The algorithm described above already provides satisfactory results (see section 3), although it is not yet particularly optimized. In the future, algorithms for severe turbulence situations will have to be studied in more detail in order to ensure optimal solutions. Other techniques, such as wave-optics approaches (e.g., Canonical Transform, Gorbunov, 2002; Full Spectrum Inversion; Jensen et al., 2003), can be used to reduce scintillation fluctuations already on the transmission measurements (Level 1b) so that less down-weighting of imaginary refractivity data will be required at the atmospheric profiles retrieval step. In particular, the use of differential transmission profiles, which are preceded in processing by a Canonical Transform step, are a most promising method to be used in case of severe turbulence (Gorbunov and Kirchengast, 2005).

As the K-band component is the novel part of GADEM, future processing advancements are possible and required at all steps of the retrieval chain: From detailed performance analyses of different methods to derive transmission profiles (both geometric-optics and wave-optics based) to optimized atmospheric profiles retrieval (both without and with presence of turbulence), future developments shall ensure exploitation of the K-band data in the best possible manner.

## *Level 1b and Level 2 Data Products*

The scientific processing discussed above provides conversion of basic geo-located Level 1 data (phase delays/Doppler shifts and amplitudes/raw transmissions) via bending angles (L-band) or bending angles and transmissions (K-band) to Level 2 atmospheric profiles. For obtaining a closer overview on the GADEM data products available in this process at Level 1b and Level 2, the reader is referred to WegCenter/UniGraz (2006).

The product domain is foreseen global, and from 5 km to 50 km in height for most products; humidity products will be available throughout the troposphere, covering 5 km to 15 km. All Level 1b and Level 2 products will be available to users within 30 days of observation time, and part of the data also in near-real time for NWP, i.e., within 3 hrs of observation time (on a best-effort basis).

Detailed performance requirements on the scientific data products are found in the GADEM requirements tables formulated in WegCenter/UniGraz (2006). This document also provides a more detailed list of data products from Level 0 to Level 2.



## 2.4.2 Atmospheric Time Series Retrieval for Galileo-GS K-band Links

### *Phase-based Method*

The phase-based method is based on a separation of an additional phase delay GNSS signals due to the atmospheric water vapor from the total excess path delay via subtracting the zenith hydrostatic delay, which has to be mapped into the ray path direction. This additional phase delay – the so called wet delay – is a valuable meteorological signal, which is nearly proportional to the quantity of water vapor integrated along the signal path – the “slant integrated water vapor” (SIWV) (see for details, e.g., Foelsche and Kirchengast, 2001). Via a transformation, the SIWV can provide the precipitable water with an accuracy of ~1 mm (e.g., Elgered et al., 1997).

### *Amplitude-based Method*

#### *Transmission retrieval*

In contrast to the amplitude-based method using occultation data, the estimation of water vapor in Galileo-GS measurements is more difficult. In this case there is no possibility to directly obtain normalized amplitudes, since the ray path is always propagating through the whole atmosphere – from space via the water vapor “contaminated” troposphere to the ground station (i.e., there is no “above the atmosphere” calibration situation). Hence, the accurate link budget – transmitter power, antennae characteristics, space loss, etc. (cf. subsection 2.3.1) – has to be known to obtain accurate values for the transmissions at the different frequencies, which are due to the total atmospheric loss only. Favorably, such accurate knowledge of relevant parameters will be available for the designed K-band system, since the link budget is very accurately known from the geometry and the system design. We use differential transmissions only (i.e., F2–F1 difference or F3–F1 difference), which provides significant advantage in that effects (e.g., drifts) common to different frequencies neatly cancel out.

#### *Slant integrated water vapor retrieval*

This step starts with the differential transmission profiles from atmospheric loss only obtained in the transmission retrieval step above. In the present algorithm used for this study, the Millimeter-wave Propagation Models (MPM) (e.g., Liebe et al., 1993) is utilized in the forward modeling of the process to optimally obtain water vapor profiles. We used as background climatological temperature and pressure profiles from the CIRA86aQ climatology (Kirchengast et al., 1999). These profiles were adjusted with an offset so as to match the surface temperature and surface pressure “measured” at the ground station (in case of the present study assuming a simulated measurement with typical measurement errors).

The optimal water vapor retrieval is then based on the comparison of the differences between two “measured” transmissions (i.e., forward modeled at two GADEM frequencies incl. errors) and two modeled transmissions (i.e., from involving an iterated water vapor profile in the retrieval algorithm, starting with a “dry-air” first guess, i.e., zero water vapor). The finally obtained water vapor profile (after minimizing the measured-minus-modeled difference and reaching adequate convergence) is used to integrate it to the estimated SIWV, via utilizing Simpson trapezoidal integration rule. Like in the phase-based case, the SIWV can then be transformed into precipitable water (e.g., Elgered et al., 1997) if desired.

(intentionally left blank; back page if double-sided print)

### 3 Performance Analysis Results

As a quasi-realistic performance analysis case an operational T511L91 analysis (~40 km x 40 km horizontal resolution, 91 vertical levels from surface to 0.01 hPa) of the ECMWF was used (12 UT analysis of March. 15, 2006; near-equinox date, otherwise arbitrarily chosen). A global set of about 180 occultation events was simulated (the number limited by the computationally expensive forward modeling as in the previous subsection), drawing every 3<sup>rd</sup> event from a day of K-band measurements, and sorting the events into three latitude bands (northern and southern hemisphere and tropics). Figure 13 illustrates the global distribution of the selected events falling into both cloudy and clear-air areas.

ECMWF analyses contain besides humidity and temperature also 3D liquid water and ice water cloud fields, which were included in the modeling. The vertical humidity and temperature profiles at each event location have been used, disregarding the horizontal variation about this location. This was done to clearly quantify the observational and retrieval errors and to avoid mixing in representativeness errors. The latter are small given properly defined “true” profiles (e.g., Foelsche and Kirchengast, 2004; Syndergaard et al., 2004). The present K-band end-to-end simulator could not yet supply adequate Abelian-weighted “true” profiles, however, but only vertical profiles. The 3D liquid water and ice water fields have been used as they are and contribute to the absorptive occultation/GNSS-GS signal at any location where rays pass through cloudiness.

#### 3.1 Results for the Galileo-LEO K-band Occultation System

Regarding turbulence/scintillations, the model of Kuhn was used (Kuhn, 2003; M. Sterenborg et al., ESA/ESTEC, pers. communications, 2003), with the main turbulence parameters modeled as a function of latitude based on the turbulence cases defined in Table 1. The values of  $C_{n0}^2$  and  $H_{Cn2}$  were assigned to latitudes (both North and South) of 0 deg (“sTR1”), 20 deg (“sST1”), 50 deg (“sML1”), and 70 deg (“sHL1”), complemented by the values ( $C_{n0}^2 = 3 \times 10^{-15} \text{ m}^{-2/3}$ ,  $H_{Cn2} = 1.75 \text{ km}$ ) at 30 deg to better reflect subtropical dry and weakly turbulent areas (cf. Kirchengast, 2004b). In between, linear interpolation was performed, and beyond 70 deg values were kept constant at the 70 deg values. If due to turbulence best-fit background temperatures needed to be invoked below  $z_{\text{Thres}}$  (see subsection 2.1.2 for details), temperature profiles from the ECMWF 24h forecast for the analysis time were used as “search library”, searching within a few degrees around the given event location. A conservative uncertainty of 0.75 K (near  $z_{\text{Thres}}$ ) to 2 K (near 2 km) was then attached to the best-fit profile.

**Table 1:** Parameters for cloud and turbulence scenarios.

1	“high-latitude” turbulence (“sHL1”)	$C_{n0}^2 = 1 \times 10^{-16} \text{ m}^{-2/3}$ , $H_{Cn2} = 2 \text{ km}$
2	“mid-latitude” turbulence (“sML1”)	$C_{n0}^2 = 1.3 \times 10^{-15} \text{ m}^{-2/3}$ , $H_{Cn2} = 2 \text{ km}$
3	“subtropical” turbulence (“sST1”)	$C_{n0}^2 = 1 \times 10^{-14} \text{ m}^{-2/3}$ , $H_{Cn2} = 1.5 \text{ km}$
4	“tropical” turbulence (“sTRI”)	$C_{n0}^2 = 2 \times 10^{-13} \text{ m}^{-2/3}$ , $H_{Cn2} = 1 \text{ km}$

**Legend:**  $C_{n0}^2$  ... turbulence structure constant at surface,  $H_{Cn2}$  ... scale height of turbulence structure constant. The horizontal extend of turbulence was set to 200 km in all cases and the vertical  $C_n^2$  decay was assumed exponential with the scale height  $H_{Cn2}$ . The outer scale of turbulence was set to 100 m.

Figures 13 to 17 show the performance results for the three latitude bands (cf. subsection 2.1.1 for detail), each containing an ensemble of about 60 occultation events (see Figure 13). Not all profiles reach fully down to 5 km, partly due to topography, partly due to multipath effects in the lower troposphere limiting the ray-tracing. Future more elaborated (and computationally expensive) wave-optics forward modeling will cope with the latter effects. From L-band experience, the performance found here using ray-tracing forward modeling will not change much, however; tentatively it will be improved.

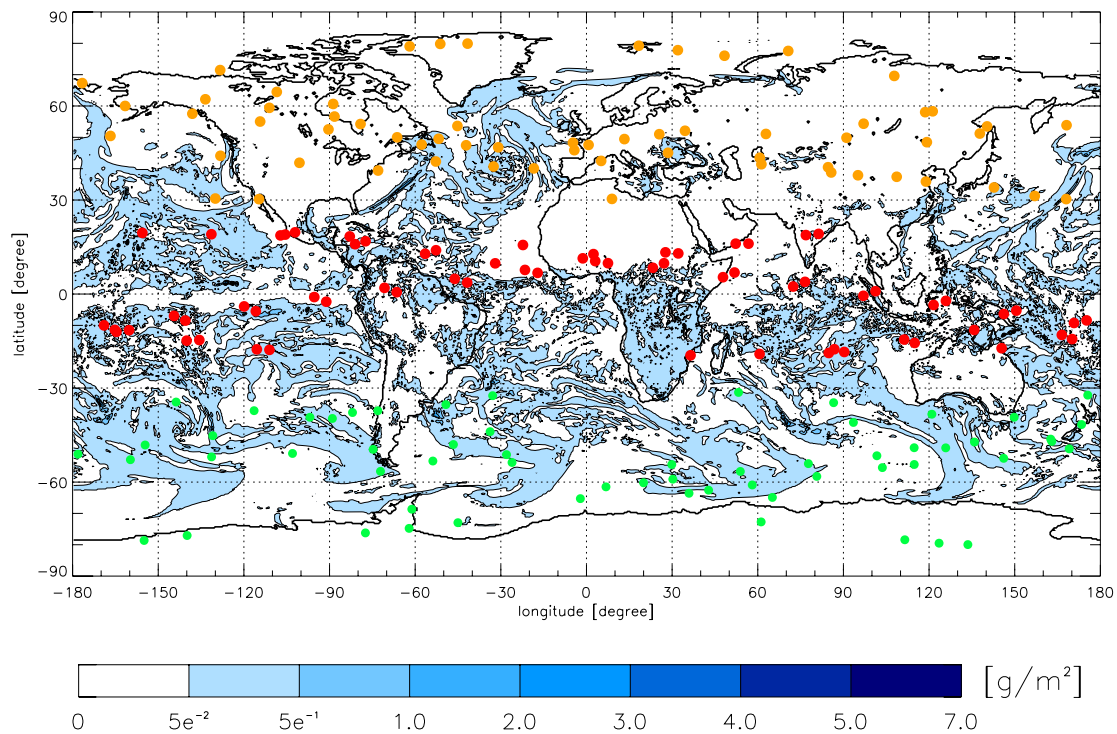


**Fig 13.** Coverage used in the simulations. In the tropical region ( $-20^\circ$  to  $20^\circ$  – red dots) each daily event, in the extratropical regions – southern hemisphere ( $-30^\circ$  to  $-90^\circ$  – green dots) and northern hemisphere ( $30^\circ$  to  $90^\circ$  – dark yellow dots) – each 3<sup>rd</sup> daily event was used. The background shows the vertically integrated liquid water density [ $\text{g}/\text{m}^2$ ], indicating cloud coverage (data from March 15, 2006, 12 UT, ECMWF analysis).

Figures 14 and 15 show the retrieval results for temperature and humidity for the extratropical northern hemispheric ensemble ( $30^{\circ}$  to  $90^{\circ}$ ) for two (F1, F3) and optionally three (F1, F2, F3) frequencies, respectively. In Figure 14 the results produced with a differential transmission retrieval are illustrated whereas in Figure 15 the absolute transmission was used to perform the retrieval for the atmospheric data products. The error scenario used was: thermal noise,  $C/N_0$  66 dBHz at 25 km, ampl. drift 0.5%/20 sec.

It can be clearly seen that the usage of three frequencies, i.e., including the optional F2 frequency, results in a better retrieval performance – particularly in the tropospheric region. Especially in the case of using two frequencies and the differential retrieval, temperature and humidity exhibit a large bias starting at about 9 km downwards, due to the fact that the 22.6 GHz frequency is attenuated already at relatively high altitudes and thus there is not enough information to separate the information of temperature and humidity contained in the signal. In practice it is thus advisable to adopt three frequencies for ensuring best retrieval performance of occultation profiles. For a GADEM demonstration experiment, however, also two frequencies could in principle show all aspects of feasibility and potential of the method. An operational system should preferably have implemented three frequencies.

Figures 16 and 17 and Figures 18 and 19 are illustrating the results for the southern hemispheric ensemble ( $-90^{\circ}$  to  $-30^{\circ}$ ) and the tropical ensemble ( $-20^{\circ}$  to  $20^{\circ}$ ), respectively, in the same way as shown in Figures 14 and 15 for the northern hemispheric ensemble. The conclusions above on the use of two vs. three frequencies are also confirmed by these results for the southern hemisphere and tropical ensemble. In particular the tropical ensemble, where tropospheric moisture concentrations are highest, highlights the utility of three frequencies. The differential retrieval mode may generally be used in case of significant atmospheric turbulence, whereas the absolute transmission profiles can be used in case of small or negligible turbulence (cf. Gorbunov and Kirchengast, 2005).

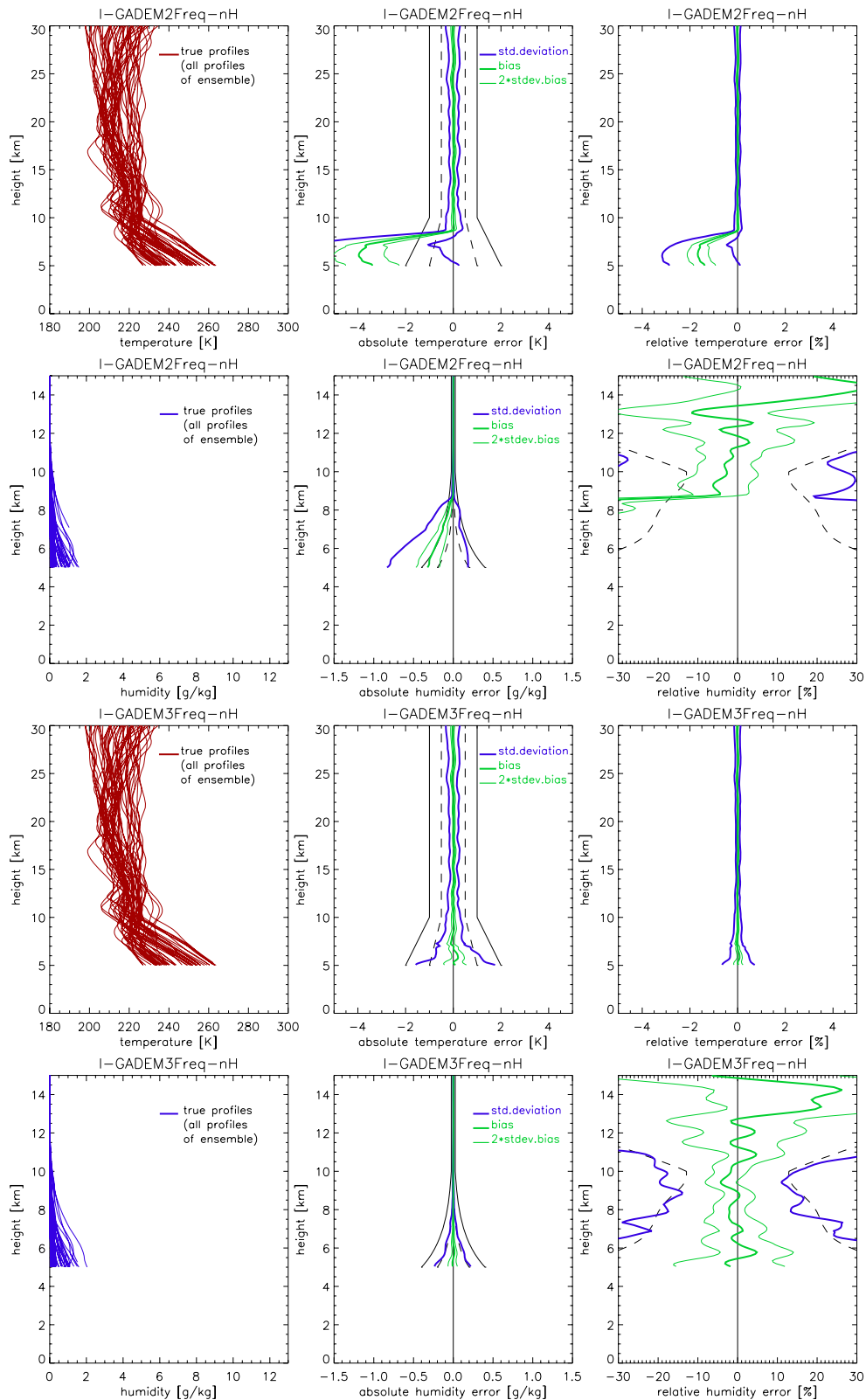


**Fig 14.** Differential transmission retrieval results for temperature and humidity for the two GADEM frequencies (F1, F3; first two rows) and for three frequencies, including the optional F2 = 20.2 GHz frequency (last two rows). The plots show the results for the northern hemisphere (30° to 90°). For more information, see text.

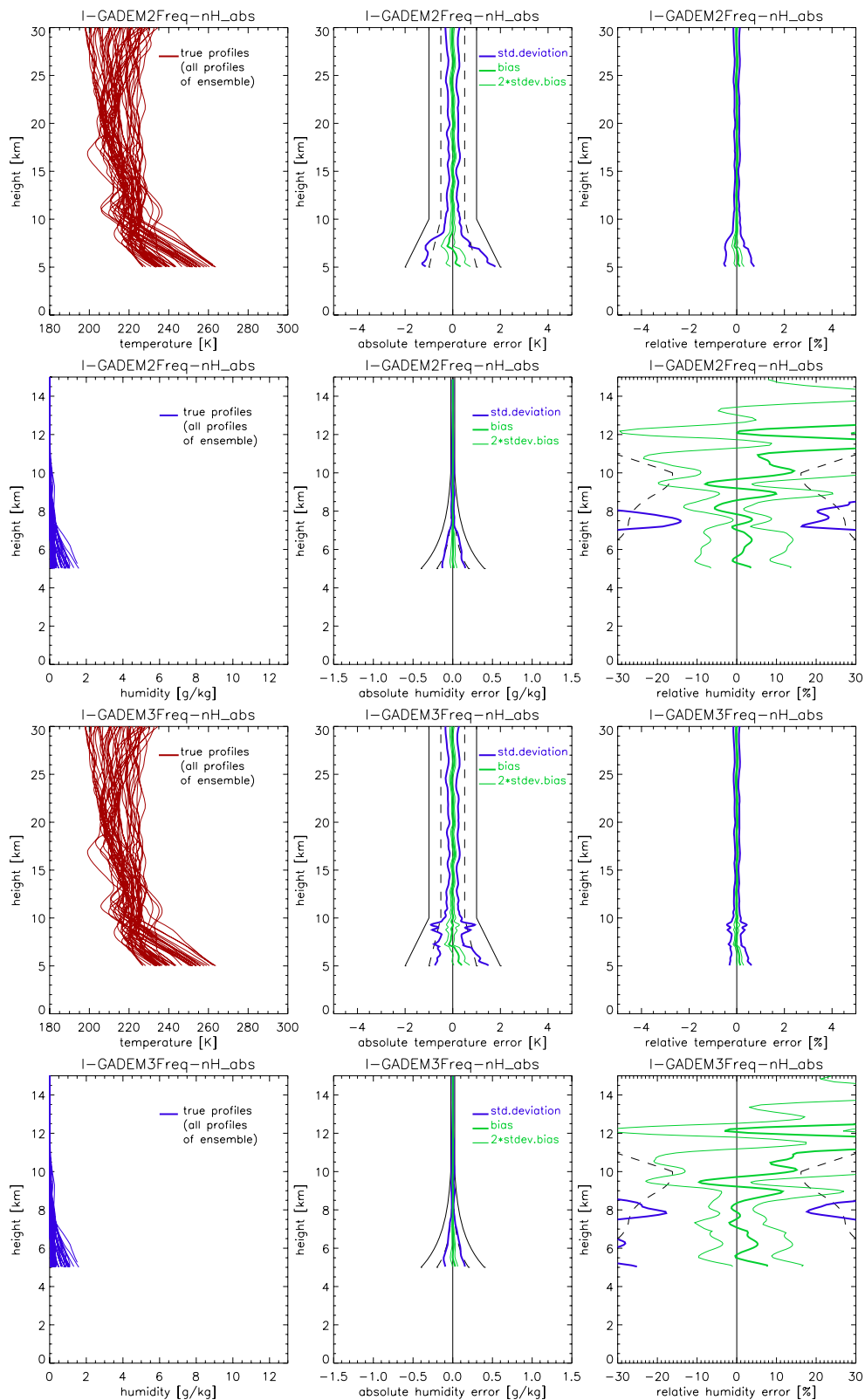


**Fig 15.** Absolute transmission retrieval results for temperature and humidity for the two GADEM frequencies (F1, F3; first two rows) and for three frequencies, including the optional F2 = 20.2 GHz frequency (last two rows). The plots show the results for the northern hemisphere (30° to 90°). For more information, see text.

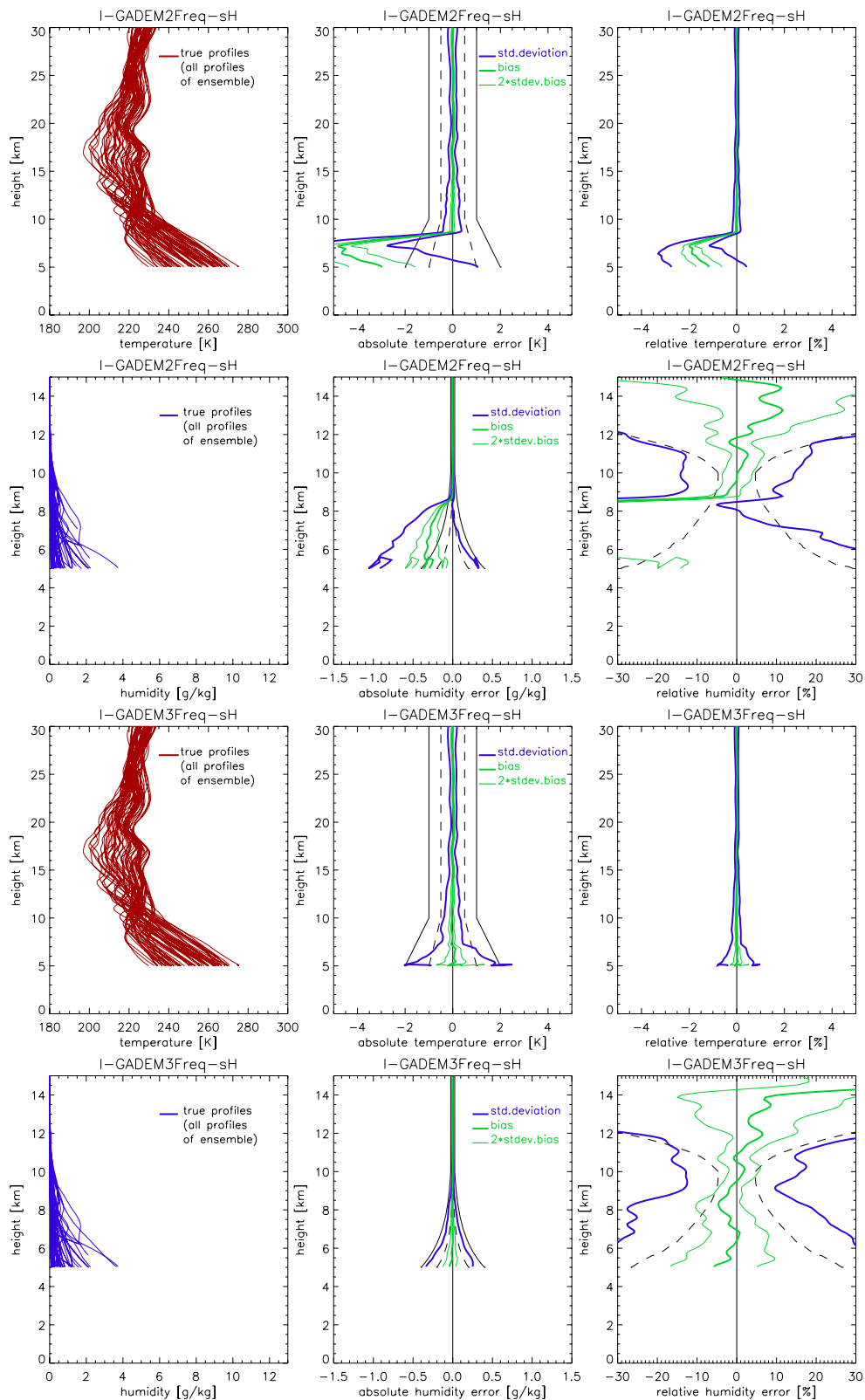


**Fig 16.** Differential transmission retrieval results for temperature and humidity for the two GADEM frequencies (F1, F3; first two rows) and for three frequencies, including the optional F2 = 20.2 GHz frequency (last two rows). The plots show the results for the southern hemisphere (-90° to -30°). For more information, see text.



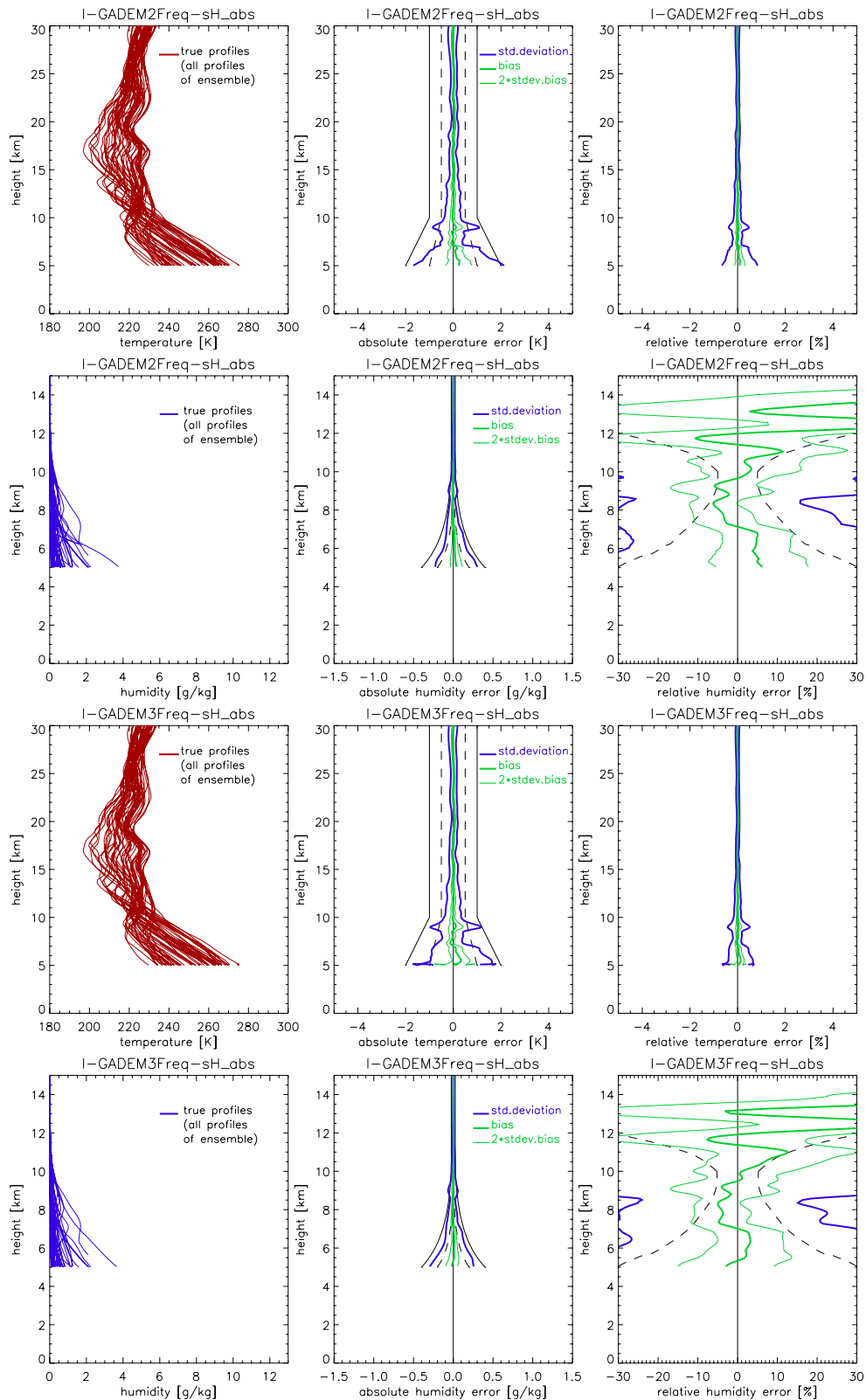


**Fig 17.** Absolute transmission retrieval results for temperature and humidity for the two GADEM frequencies (F1, F3; first two rows) and for three frequencies, including the optional F2 = 20.2 GHz frequency (last two rows). The plots show the results for the southern hemisphere (-90° to -30°). For more information, see text.

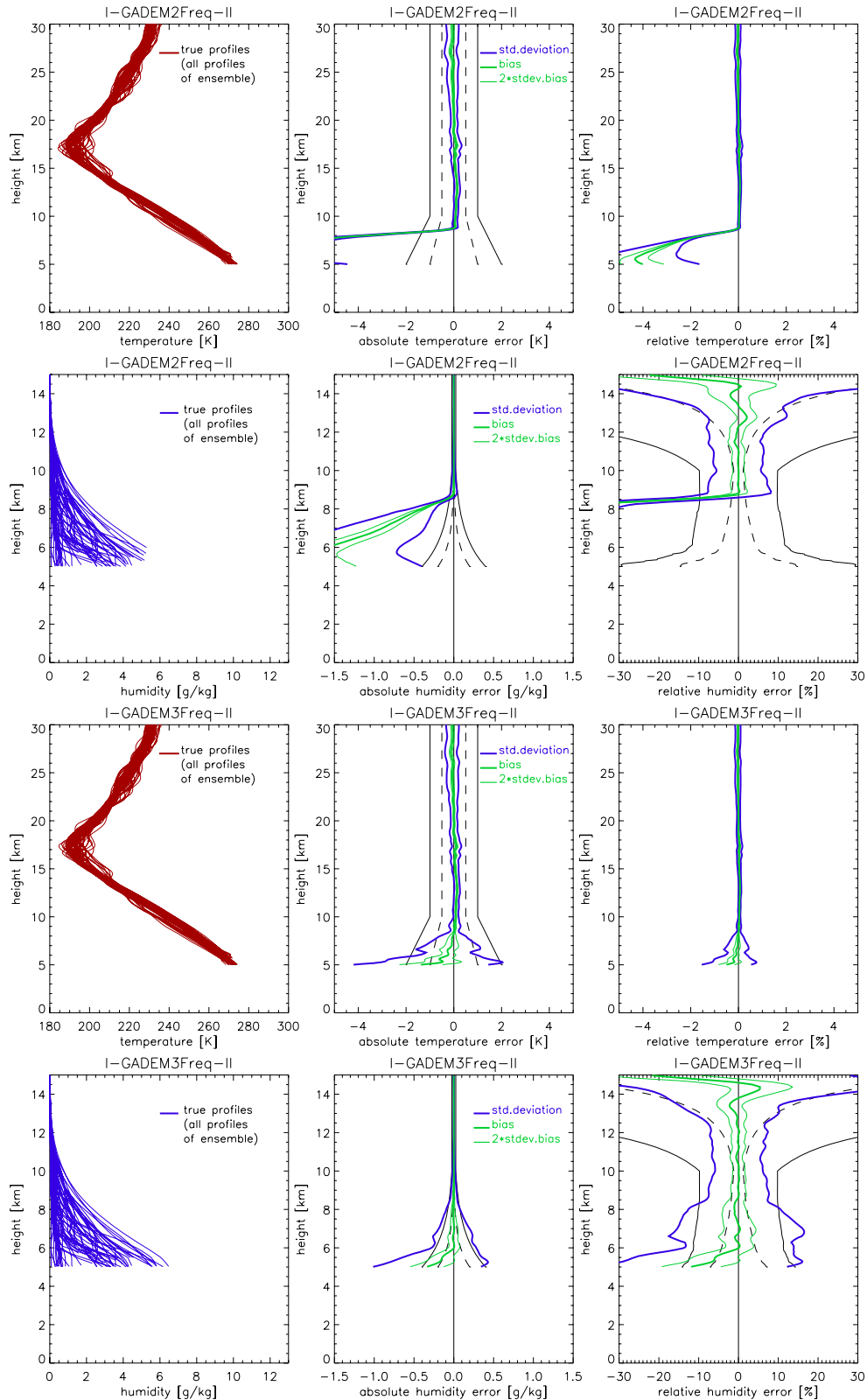


**Fig 18.** Differential transmission retrieval results for temperature and humidity for the two GADEM frequencies (F1, F3; first two rows) and for three frequencies, including the optional F2 = 20.2 GHz frequency (last two rows). The plots show the results for the tropics ( $-20^\circ$  to  $20^\circ$ ). For more information, see text.

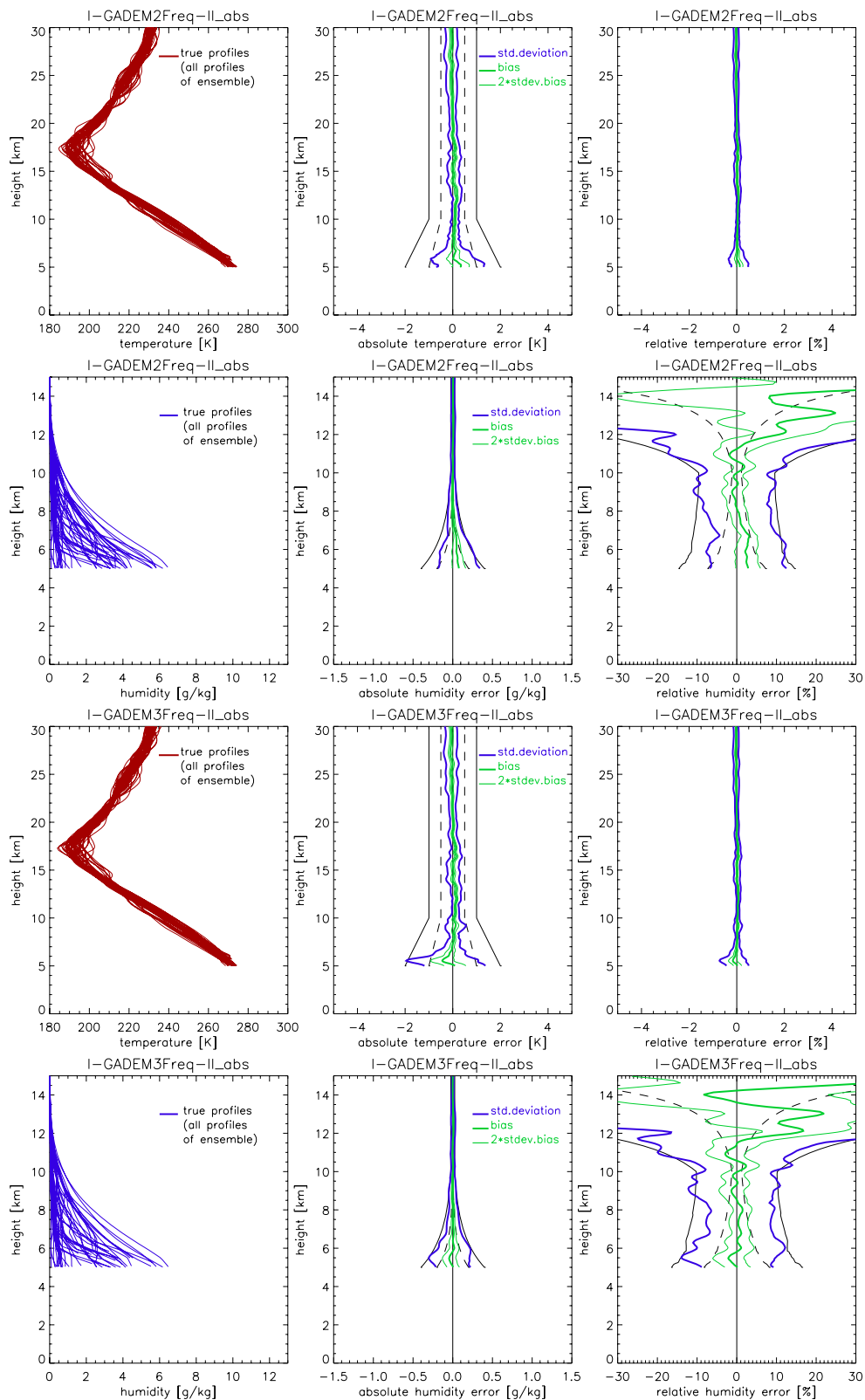


**Fig 19.** Absolute transmission retrieval results for temperature and humidity for the two GADEM frequencies (F1, F3; first two rows) and for three frequencies, including the optional F2 = 20.2 GHz frequency (last two rows). The plots show the results for the tropics ( $-20^\circ$  to  $20^\circ$ ). For more information, see text.

(intentionally left blank; back page if double-sided print)

### 3.2 Results for the Galileo-GS System

Regarding the surface pressure and surface temperature at the location of the ground station, which are used in both the phase-based and the amplitude-based retrieval method, it has to be noted that a Gaussian noise of 0.5 hPa in pressure and 0.2 K in temperature was superposed to those values, accounting for the typical errors of the respective measuring sensors.

Figure 20 shows the distribution of the utilized ensemble of ground stations over a map illustrating the vertically integrated total column content of water vapor [ $\text{kg}/\text{m}^2$ ] for March 15, 2006, 12 UT, obtained from an ECMWF analysis. For each of the 10 ground stations (GS), a sample of 4 events was selected, with a duration time of the Galileo-GS scan per event of at least 90 minutes.

The Galileo-GS performance results are shown in Figures 21 to 25, where the SIWV error [%] is shown, computed relative to the “true” SIWV (known from integration through the ECMWF analysis water vapor field without superposing any errors). The data analyzed were five-minute averaged samples of the raw retrieved data, which were assumed measured at a sampling rate of 0.1 Hz (10 sec data). This 5-min sampling reflects the Galileo-to-GS target sampling requirement as expressed in the WegCenter/UniGraz (2006) requirements.

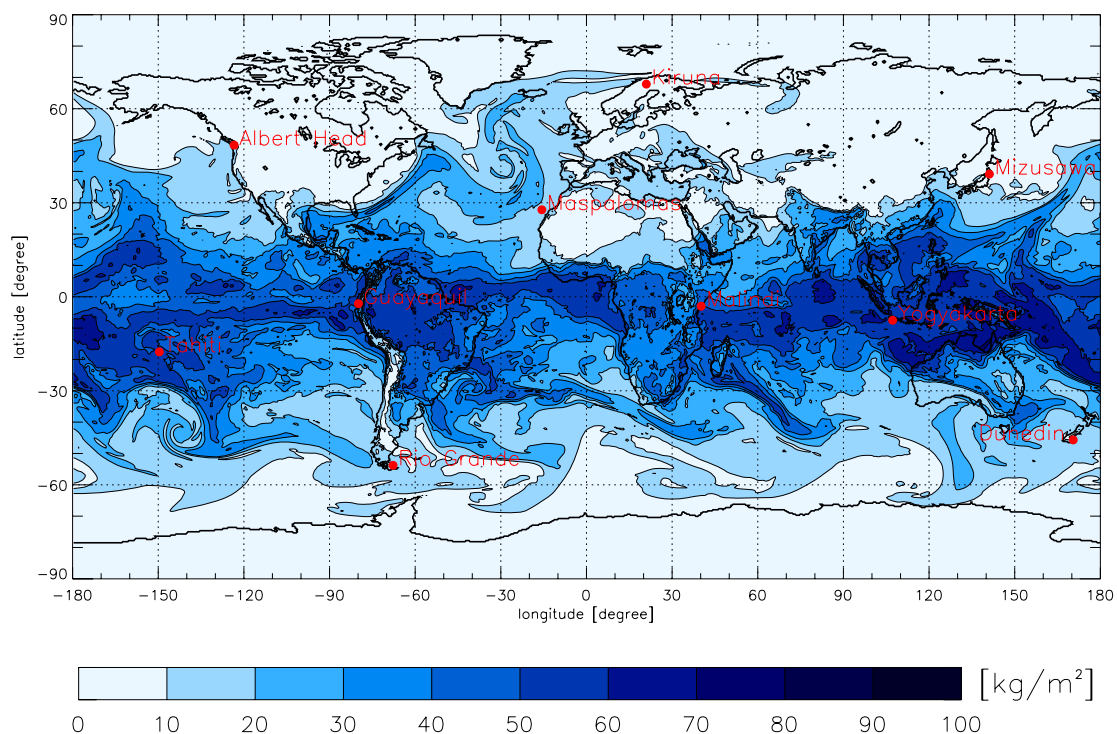


**Fig 20.** The red dots illustrate the 10 ground stations used in the Galileo-GS simulations. The background shows the vertically integrated water vapor density [ $\text{g}/\text{m}^2$ ] (data from March. 15, 2006, 12 UT, ECMWF analysis).

Figures 21 and 22 are illustrating exemplary GNSS-GS retrieval results for a Galileo-GS event received at the ground stations Malindi (Kenya) and Kiruna (Sweden), respectively. These are two opposed cases – the first one, Malindi, is located in the tropics, which means that we can expect a high SIWV content (very moist air) whereas the second one, Kiruna, is a polar station, i.e., the SIWV content will be low.

It can be clearly seen that in the case of the amplitude-based retrieval method for Malindi, the results for the retrieval using the F1 and F2 frequency are very good. On the other hand we obtain a bias for the retrieval using the channels F1 and F3, which depends slightly on the elevation angle. This latter bias has its roots in the fact that the F1 and F3 frequencies are fairly widely separated ( $> 5$  GHz from 17.25 GHz to 22.6 GHz) so that the differential amplitude is more vulnerable to liquid water contributions in the atmosphere, which leave a residual bias. “No retrieval” is possible in case of the amplitude-based method if the transmission difference between the frequencies is too small to enable accurate determination of the SIWV (i.e., in case of very low water vapor content).

Regarding the phase based retrieval it can be seen that there occurs no bias, neither in the case using the channels F1 and F2 nor using F1 and F3, since phase is related to the non-dispersive refractivity only (combination of two channels in the case of the phase-based retrieval means that two frequencies have to be used to cancel out the ionospheric effects). However, in both phase-based cases the differences compared to the true SIWV content are higher than in the amplitude-based case, indicating the potential of adding K band signals for enabling amplitude-based retrievals in addition to phase-based retrievals.

Inspecting the results of the station Kiruna we have to keep in mind that the total SIWV content can be expected to be quite small compared to Malindi. This results in a less robust retrieval and therefore in higher fluctuations of the errors for both the phase-based case and for the amplitude-based case, using the channels F1 and F2 in the retrieval. The amplitude-based case using F1 and F3 provides an interesting result: The bias which is present also at the Malindi station remains, but the error fluctuations when comparing to the retrieval using F1 and F2 are smaller. The reason for the latter is that the difference in attenuation is larger between F1 and F3 and therefore the influence of the noise is decreasing compared to the F1 and F2 case.

Figures 23 and 24 present the results for the error analysis for two interesting cases of dependencies of the errors: In Figure 23 we present the results (bias, standard deviation, and standard deviation of bias) depending on the elevation angle and in Figure 24 depending on the (“true”) total SIWV content, respectively. Showing the errors in form of these dependencies is more instructive than just inspecting time series errors.

Examining the results for the elevation-angle based plots (Figure 23) we can see that in the amplitude-based retrieval the combination of the channels F1 and F2 leads to a higher deviation (higher standard deviation) but less biased result than combining F1 and F3. The reason that the largest biases do not arise at nearly vertical measurements ( $\sim 90^\circ$  in elevation) is that those measurements of the sample with high elevation lie in regions where the total SIWV content is also high, which cancels out the elevation effect. Note that the station Kiruna, which is the station with the lowest total SIWV, lies at about  $68^\circ\text{N}$  and therefore the

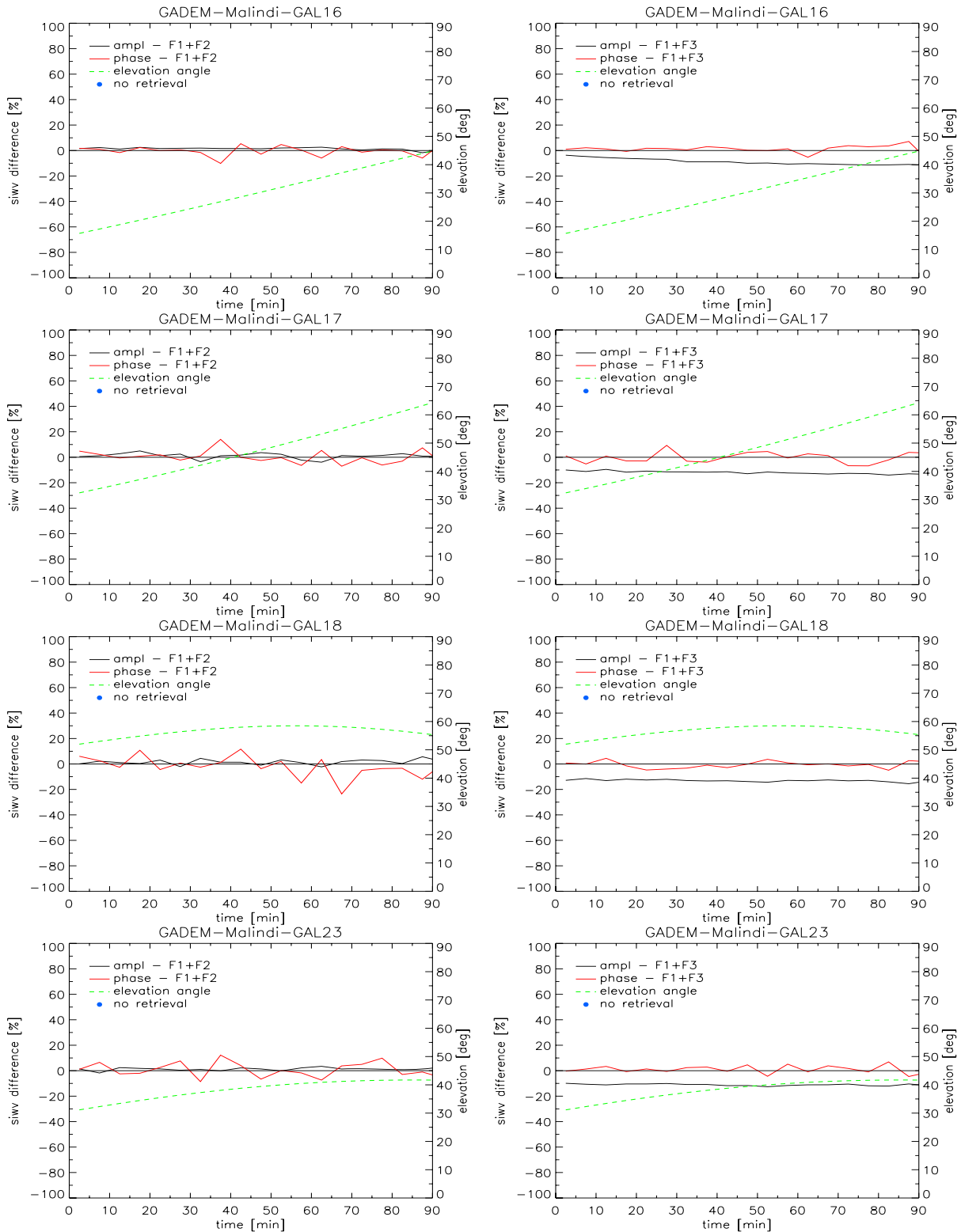
elevation angle could never reach  $90^\circ$ , since the highest latitude reached by the Galileo satellites (sub-orbital track) lies at about  $56^\circ$ .

Another instructive view on the amplitude-based retrieval can be found in Figure 24, where the errors are plotted against the total SIWV content. Here we can see that there are really small standard deviations in both cases (using F1 and F2 or using F1 and F3). Biases are present, e.g., due to residual liquid water effects. They reside within 5-10%, however.

For both cases, the phase-based retrieval exhibits a positive bias for small elevation angles resulting from an imperfect retrieval due to the decrease in performance of the used “geometric” mapping function (cf. Foelsche and Kirchengast, 2001) for small elevation angles.

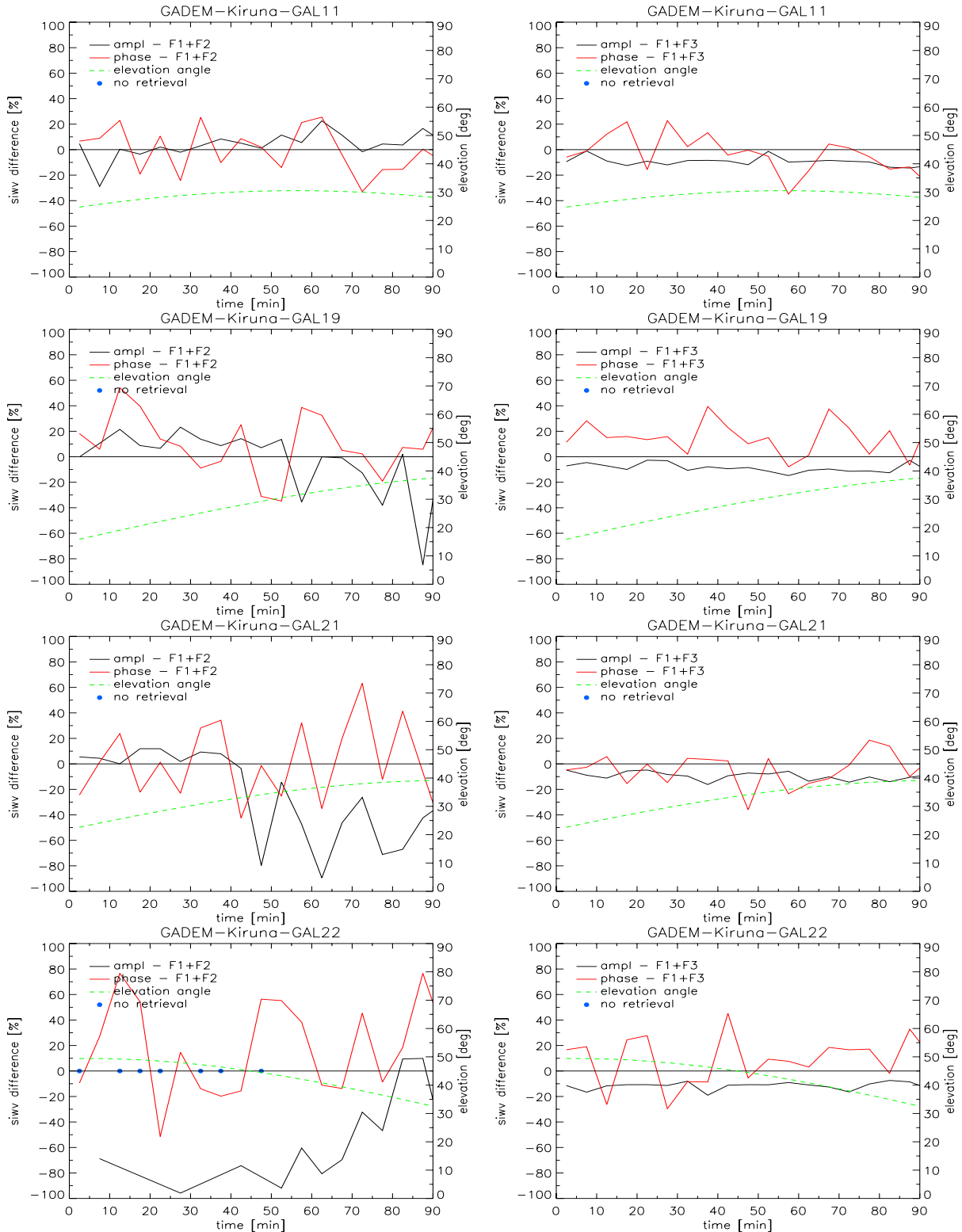
In summary it can be said that both Figures, Figure 23 as well as Figure 24, show that the target requirement accuracy of 5% in total SIWV for 5-min samples (WegCenter/UniGraz, 2006) can be reached by a combination of the amplitude-based and the phase-based method. In the upper left panel of Figure 24 it is also illustrated that even using the amplitude-based method alone the accuracy level of 5% is reachable for almost the whole spectrum of total SIWV content except for very low ones. The superior result for the combined use of phase-based and amplitude-based retrieval underpins the utility of the K-band compared to the L-band, since only in K-band the additional amplitude-based retrieval is available.

Figure 25, finally, shows the performance analysis results for the case that an additional linear phase drift error of 3 mm/min is randomly superposed on the phase (lasting over the full 5-min sample, by the same method as illustrated in Fig. 9 for the amplitude drift). It can be seen that this additional phase drift error has almost no effect on the retrieval results. The small differences which do occur are in fact more a result of the different random (thermal) phase errors superposed in both cases. This shows that phase drifts will in general not be a concern for a GADEM system, since a design limiting phase drifts to say  $< 3 \text{ mm}/30 \text{ sec}$  (i.e., twice the value tested in Figure 25, which is still no concern) is not challenging and already existing from L band heritage.



**Fig 21.** Exemplary Galileo-GS retrieval results for the ground station Malindi (Kenya). The left panels are illustrating the results when using the F1 and the optional F2 frequency for the retrieval, the right panels illustrate the results for the two main GADEM frequencies F1 and F3. The black line shows the errors of the retrieved SIWV [%] for using the amplitude-based method, the red line the results for the phase-based method. Additionally, the evolution of the elevation angle during the event is shown (dashed green line). The blue dots indicate samples (if any) where no retrieval could be utilized in the amplitude-based case.





**Fig 22.** Exemplary Galileo-GS retrieval results for the ground station Kiruna (Sweden). The left panels are illustrating the results when using the F1 and the optional F2 frequency for the retrieval, the right panels illustrate the results for the two main GADEM frequencies F1 and F3. The black line shows the errors of the retrieved SIWV [%] for using the amplitude-based method, the red line the results for the phase-based method. Additionally, the evolution of the elevation angle during the event is shown (dashed green line). The blue dots indicate those samples where no retrieval could be utilized in the amplitude-based case.

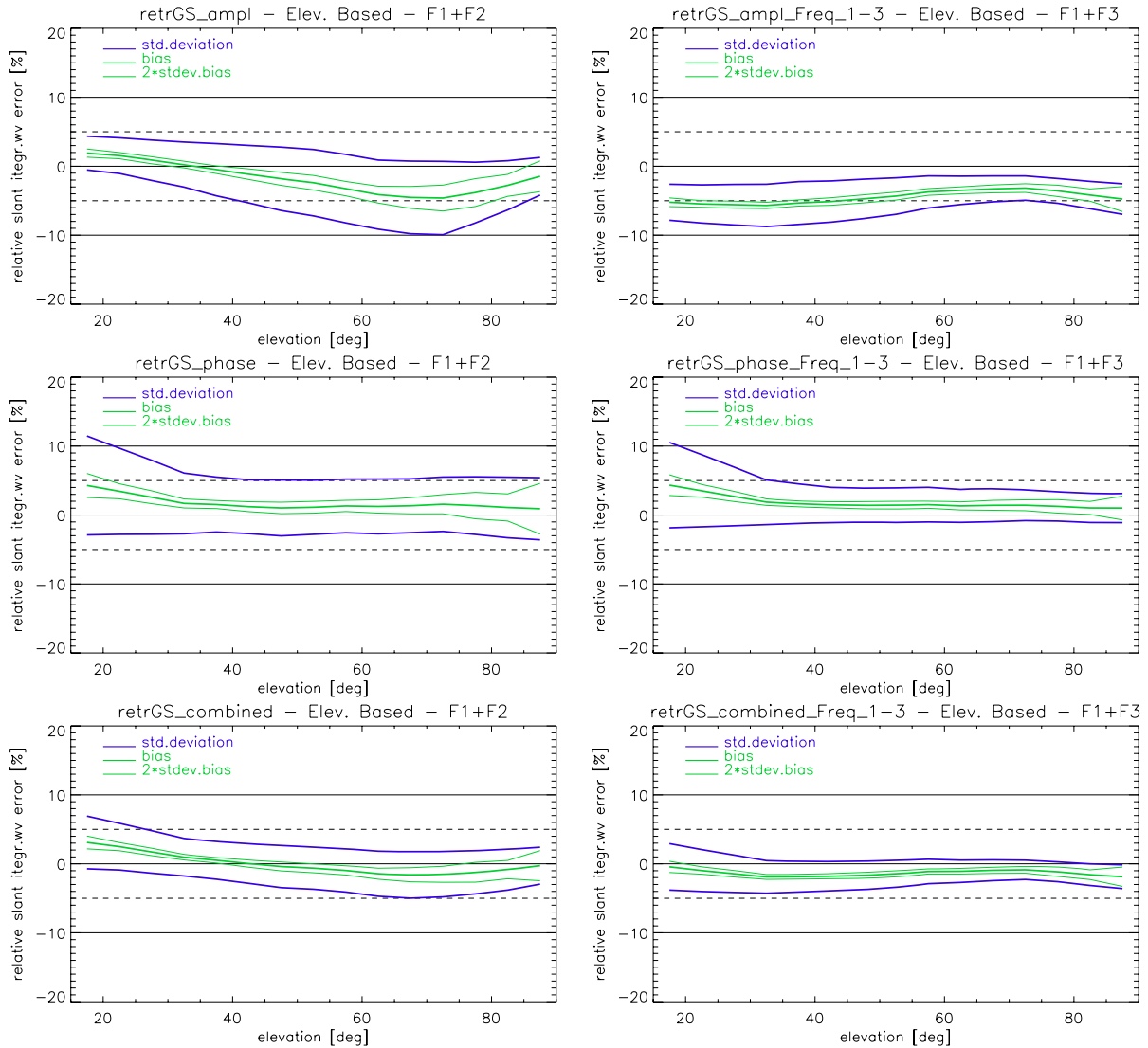


**Fig 23.** Results for the SIWV retrieval errors [%] as a function of the elevation angle. The left panels are illustrating the results when using the F1 and the optional F2 frequency for the retrieval, the right panels illustrate the results for the two main GADEM frequencies F1 and F3. The first row shows the errors for the amplitude-based method, the second row those for the phase-based method, and the third row the results when combining both methods.

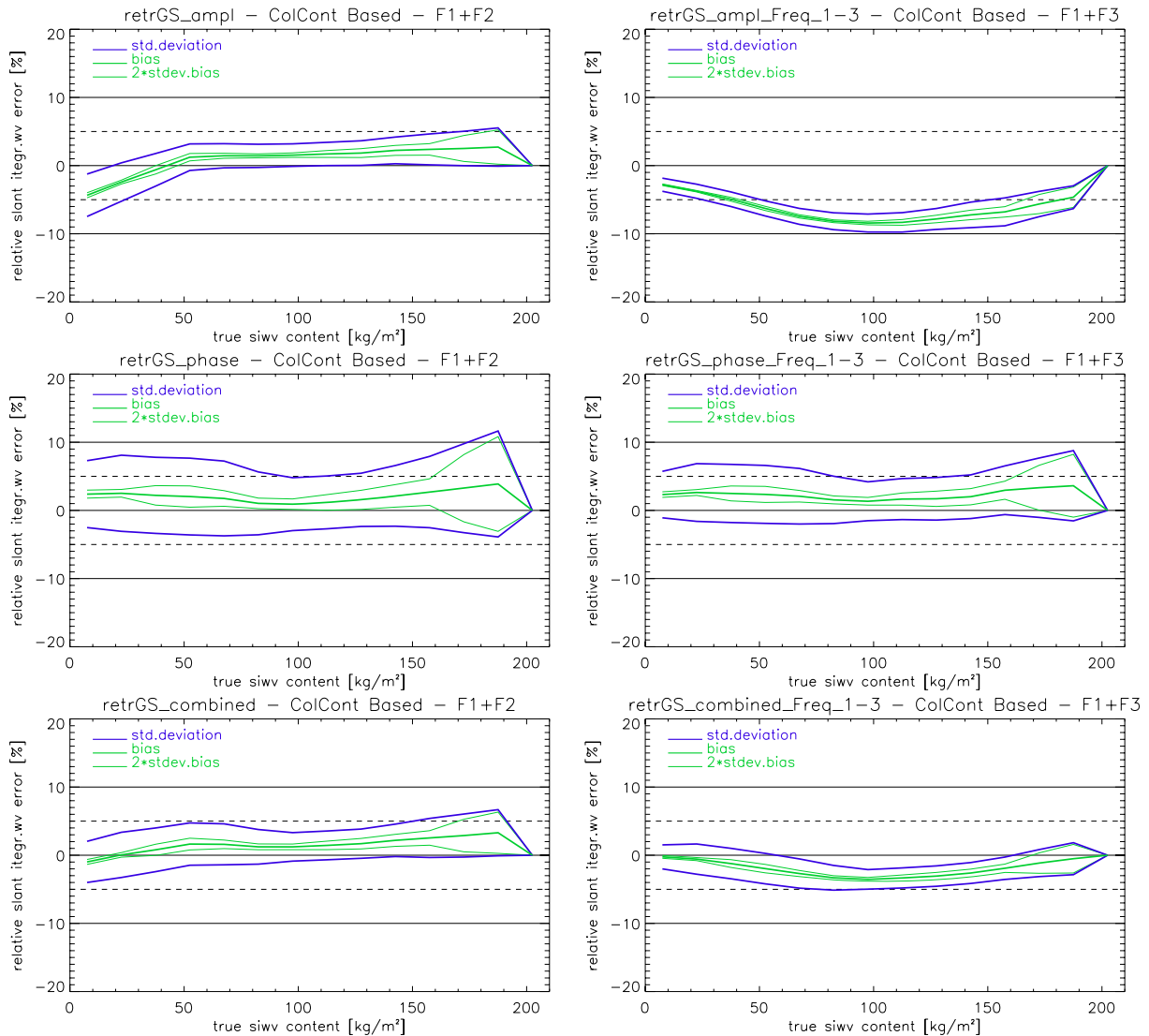


**Fig 24.** Results for the SIWV retrieval errors [%] as a function of the “true” total SIWV content. The left panels are illustrating the results when using the F1 and the optional F2 frequency for the retrieval, the right panels illustrate the results for the two main GADEM frequencies F1 and F3. The first row shows the errors for the amplitude-based method, the second row those for the phase-based method, and the third row the results when combining both methods.

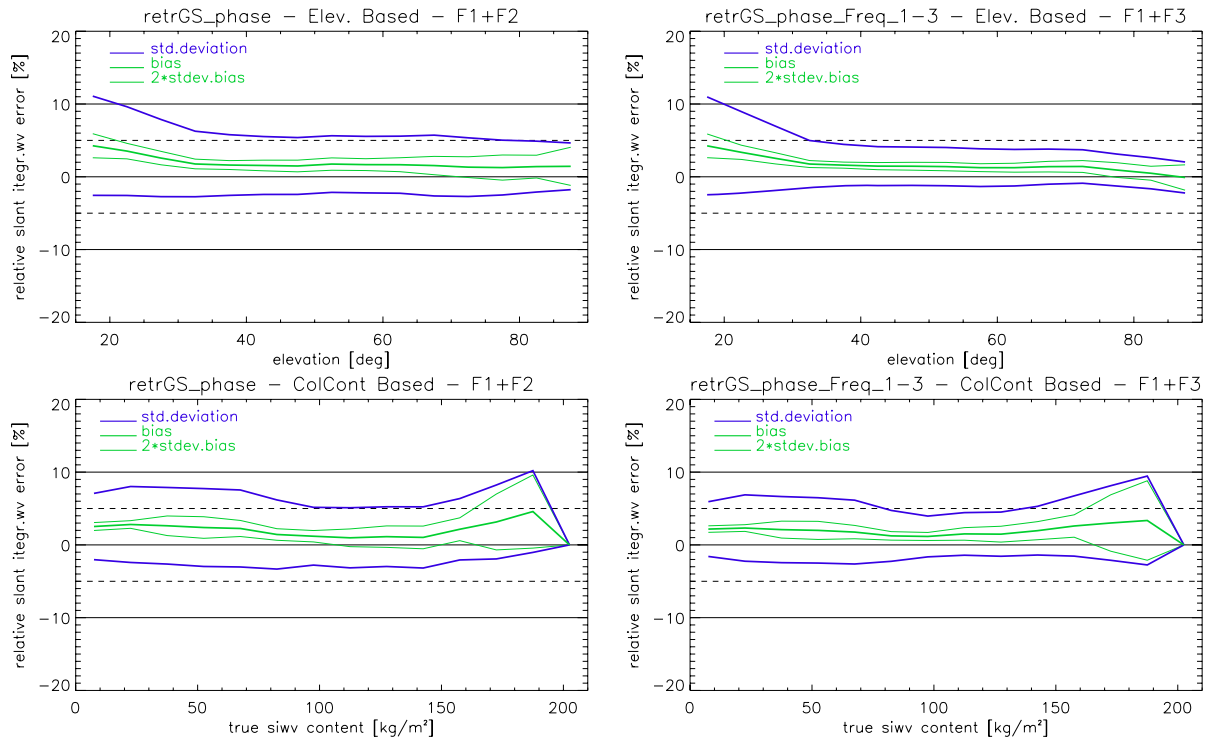


**Fig 25.** Results for the SIWV retrieval errors [%] for the phase-based case including an additional phase drift error of 3 mm/min. The left panels are illustrating the results when using the F1 and the optional F2 frequency for the retrieval, the right panels illustrate the results for the two main GADEM frequencies F1 and F3. The first row shows the errors dependent on the elevation angle, the second row shows the errors depending on the “true” total SIWV content.

## 4 Conclusions and Outlook

This study addressed the quality of atmospheric data products expected by a GADEM-type measurement configuration. The performance analysis covered a Galileo-LEO part (occultation measurements of temperature and humidity profiles) as well as a Galileo-GS part (space-to-ground slant column integrated water vapor measurements). Based on a comprehensive end-to-end simulation software, the performance of both these measurement configurations was simulated and analyzed for a typical set of instrumental errors, using realistic orbital and ground-station geometries and using as a realistic atmospheric model a high resolution ECMWF analysis field including also liquid water and ice water clouds. In addition, turbulent atmospheric conditions were taken into account for Galileo-LEO links.

The main conclusion of the study is that the GADEM system requirements as laid in the GADEM Scientific Applications document (WegCenter/UniGraz, 2006) are just adequate to achieve the observational requirements (summarized in the same document) for both the Galileo-LEO part and the Galileo-GS part, respectively. This confirms that those requirements, in many aspects drawing from heritage from previous study of similar systems (e.g., LEO-LEO K band occultation; Kirchengast and Hoeg, 2004) provide a sound basic set of specifications for GADEM system design.

More specifically, the Galileo-LEO K-band performance was found fully compliant with the requirements laid out in WegCenter/UniGraz (2006) for Galileo-LEO K-band radio links, in most cases also with the target requirements down to 5 km. Compared to the well known L-band links (“GPS occultation”) with their ambiguity in tropospheric temperature and humidity, the consistent availability of accurate humidity, temperature, and pressure as a function of height from K-band is a particularly attractive property of K-band occultation. The performance results furthermore demonstrated the essentially bias-free character of the K-band occultation retrieval products. This key characteristic is based on the favorable self-calibrating nature of the Galileo-LEO measurements.

Concerning the Galileo-GS radio link it was found that the requirements laid out in WegCenter/UniGraz (2006) were reliably reached, in most cases to target requirements, when using the information of amplitude and phase together. This superiority of the performance when including amplitude information, which is available from K band but not from L band, underpins the substantial added-value of K band signals also for Galileo-GS links, strongly complementing the added-value for Galileo-LEO links.

Regarding the use of two frequencies only (17.25 GHz and 22.6 GHz), compared to the use of three frequencies (including a third frequency near 20.2 GHz), the clear finding was that three frequencies deliver performance advantages (improved retrieval accuracy) for both Galileo-LEO and Galileo-GS links. For a future operational GADEM-type system thus three frequencies are recommended. For a GADEM demonstration experiment, however, also two frequencies could basically show all aspects of feasibility and potential of the method.

Based on the encouraging results of this performance analysis we strongly recommend a GADEM demonstration mission.

**Acknowledgments.** The authors thank J. Fritzer (WegCenter/Univ. of Graz) for his support in using the EGOPS5 software. The EGOPS5 software, the core tool of the performance analysis, was developed by an international consortium led by Univ. of Graz and involving partner teams at Danish Meteorological Institute, Denmark, Chalmers University of Technology, Sweden, and University of Bremen, Germany, and all Colleagues in these partner teams are thanked for their contributions. EGOPS5 is based on strong heritage from EGOPS4, which was developed 1996–2003 by a consortium led by Univ. of Graz and involving partner teams at Danish Meteorological Institute and TERMA Elektronik A/S, Denmark, the Met. Office, U.K., and Austrian Aerospace GmbH, Austria, with the major funding provided by ESA. The European Centre for Medium-Range Weather Forecasts (ECMWF) is acknowledged for access to atmospheric analysis data.

The work was performed under contract GJU/06/2423/CTR/GADEM of the Galileo Joint Undertaking (GJU). The work of M. Schwaerz and J. Ramsauer (WegCenter) was partially funded also by the ESA Prodex Arrangement No. 90152-CN1 (Project Advanced Topics in RO Modelling and Retrieval) for which the analysis aided to assess, as part of EGOPS5 software enhancements, the relative retrieval performance of single-channel transmission processing and the newly developed differential transmission processing, respectively.

## References

- Elgered, G., J.M. Johansson, B.O. Rönnäng, and J.L. Davis (1997), Measuring regional atmospheric water vapor using the Swedish permanent GPS network, *Geophys. Res. Lett.*, 24, 2663–2666.
- Foelsche, U., and G. Kirchengast (2002), A simple “geometric” mapping function for the hydrostatic delay at radio frequencies and assessment of its performance, *Geophys. Res. Lett.*, 10.1029/2001GL013744, 111-1 – 111-4. [on-line: [www.wegcenter.at](http://www.wegcenter.at) > Research > ARSCLiSys Research Group > Publications]
- Foelsche, U., and G. Kirchengast (2004), Sensitivity of GNSS occultation profiles to horizontal variability in the troposphere: a simulation study, *Proc. Book, 1st Int'l Workshop on Occultations for Probing Atmosphere and Climate (OPAC-1)*, Sept. 2002, Graz, Austria, Springer Verlag. [on-line: [www.wegcenter.at](http://www.wegcenter.at) > Research > ARSCLiSys Research Group > Publications]
- Foelsche, U., and G. Kirchengast (2001), Tropospheric water vapor imaging by combination of ground-based and spaceborne GNSS sounding data, *J. Geophys. Res.*, 106, 27,221 – 27,231.
- Gage, K.S. (1990), Radar Observations of the Free Atmosphere: Structure and Dynamics, in *Radar in Meteorology (ed. D. Atlas), part II, chap 28*, American Met. Society (AMS) Publ., 534–565.
- Gorbunov, M.E. (2002), Canonical Transform method for processing GPS radio occultation data in the lower troposphere, *Radio Sci.*, 37, 1076, doi:10.1029/2000RS002592.
- Gorbunov, M.E., and G. Kirchengast (2005), Processing X/K band radio occultation data in the presence of turbulence, *Radio Sci.*, 40, RS6001, doi:10.1029/2005RS003263.
- Hoeg, P., A. Hauchecorne, G. Kirchengast, S. Syndergaard, B. Belloul, R. Leitinger, and W. Rothleitner (1995), Derivation of atmospheric properties using a radio occultation technique, *DMI Scient. Report 95-4*, 205 pp., Danish Meteorol. Institute, Copenhagen, Denmark.
- Jensen, A. S., M. S. Lohmann, H.-H. Benzon, and A. S. Nielsen (2003), Full spectrum inversion of radio occultation signals, *Radio Sci.*, 38, doi: 10.1029/2002RS002763.
- Kayser-Threde (2006a), GADEM Constellation Analysis Report, *GADEM Project Report No. GAD-RP-004-KT*, Kayser-Threde GmbH, Munich, Germany.
- Kayser-Threde (2006b), GADEM Mission Requirements Specification, *GADEM Project Report No. GAD-SP-005-KT*, Kayser-Threde GmbH, Munich, Germany.
- Kirchengast, G., and P. Hoeg (2004), The ACE+ Mission: An Atmosphere and Climate Explorer based on GPS, GALILEO, and LEO-LEO Radio Occultation, in *Occultations for Probing Atmosphere and Climate*, Kirchengast-Foelsche-Steiner (eds.), 201–220, Springer, Berlin-Heidelberg. [on-line: [www.wegcenter.at](http://www.wegcenter.at) > Research > ARSCLiSys Research Group > Publications]
- Kirchengast, G., J. Hafner, and W. Poetzi (1999), The CIRA86aQ\_UoG model: An extension of the CIRA-86 monthly tables including humidity tables and a Fortran95 global moist air climatology model, *Techn. Report for ESA/ESTEC No. 8/1999*, 18p., Inst. Meteorol. Geophys., Univ. of Graz, Austria. [on-line: [www.wegcenter.at](http://www.wegcenter.at) > Research > ARSCLiSys Research Group > Publications]
- Kirchengast, G., J. Fritzer, and J. Ramsauer (2002), End-to-end GNSS Occultation Performance Simulator Version 4 (EGOPS4) Software User Manual (Overview and Reference Manual), *Techn. Report for ESA/ESTEC No. 3/2002*, 472p., IGAM, Univ. of Graz, Austria. [on-line: [www.wegcenter.at](http://www.wegcenter.at) > Research > ARSCLiSys Research Group > Publications]
- Kirchengast, G., S. Schweitzer, J. Ramsauer, J. Fritzer, and M. Schwaerz (2004), Atmospheric Profiles Retrieved from ACE+ LEO-LEO Occultation Data: Statistical Performance Analysis using Geometric Optics Processing, *Tech. Report for ESA/ESTEC No. 1/2004a*, IGAM, Univ. of Graz, Austria. [on-line: [www.wegcenter.at](http://www.wegcenter.at) > Research > ARSCLiSys Research Group > Publications]

- Kirchengast, G., J. Fritzer, M. Schwaerz, S. Schweitzer, and L. Kornblueh (2004), The Atmospheric and Climate Explorer Mission ACE+: Scientific Algorithms and Performance Overview, *Tech. Report for ESA/ESTEC No. 2/2004b*, IGAM, Univ. of Graz, Austria. [on-line: [www.wegcenter.at](http://www.wegcenter.at) > Research > ARSCliSys Research Group > Publications]
- Kuhn, T. (2003), TurbScintModel – the EGOPS scintillation model for LEO-LEO occultations, *Draft Report to ESA/ESTEC-Oct.2003*, 22 p., IEP/Univ. of Bremen, Germany.
- Kursinski, E.R., S. Syndergaard, D. Flittner, D. Feng, G. Hajj, B. Herman; D. Ward and T. Yunck (2002), A microwave occultation observing system optimized to characterize atmospheric water, temperature and geopotential via absorption, *J. Atmos. Oceanic Technol.*, 19(12), 1897–1914.
- Kursinski, E. R., G. A. Hajj, K. R. Hardy, J. T. Schofield, and R. Linfield (1997), Observing the Earth's atmosphere with radio occultation measurements using the Global Positioning System, *J. Geophys. Res.*, 102(D19), 23429–23465.
- Kursinski, E.R., D. Feng, D. Flittner, G. Hajj, B. Herman, F. Romberg, S. Syndergaard, D. Ward, and T. Yunck (2004), An active microwave limb sounder for profiling water vapor, ozone, temperature, geopotential, clouds, isotopes and stratospheric winds, *Proc. Book, 1st Int'l Workshop on Occultations for Probing Atmosphere and Climate (OPAC-1)*, Sept. 2002, Graz, Austria, Springer Verlag.
- Lee, L-C., C. Rocken, and R. Kursinski (Eds.) (2001), *Applications of Constellation Observing System for Meteorology, Ionosphere, and Climate*, Springer-Verlag, Hong Kong.
- Liebe, H.J., G. Hufford, and M. Cotton (1993), Propagation modelling of moist air and suspended water/ice particles at frequencies below 1000 GHz, in *52<sup>nd</sup> Specialists Meeting of the Electromagnetic Wave Propagation Panel*, p 542, AGARD.
- Melbourne, W. G., E. S. Davis, C. B. Duncan, G. A. Hajj, K. R. Hardy, E. R. Kursinski, T. K. Meehan, L. E. Young, and T. P. Yunck (1994), The application of spaceborne GPS to atmospheric limb sounding and global change monitoring, *JPL Publication 94-18*, 147 pp., Jet Prop. Lab, Pasadena/CA, U.S.A.
- Nielsen, A.S., M.S. Lohmann, P. Høeg, H.-B. Benzon, A.S. Jensen, T. Kuhn, C. Melsheimer, S.A. Buehler, P. Eriksson, L. Gradinarsky, C. Jimenez, and G. Elgered (2003), Characterization of ACE+ LEO-LEO Radio Occultation Measurements, *ESTEC contract no. 16743/02/NL/FF*.
- Rodgers, C. (2000), *Inverse methods for atmospheric sounding: theory and practice*, 256 pp., Word Sci., River Edge, N.J.
- Steiner, A. K., G. Kirchengast, U. Foelsche, L. Kornblueh, E. Manzini, and L. Bengtsson (2001), GNSS occultation sounding for climate monitoring, *Phys. Chem. Earth (A)*, 26, 113–124.
- Syndergaard, S. (1998), Modeling the impact of the Earth's oblateness on the retrieval of temperature and pressure profiles from limb sounding, *J. Atmos. Terr. Phys.*, 60, 171-180.
- Syndergaard, S, D. Flittner, R. Kursinski, D. Feng, B. Herman and D. Ward (2004), Simulating the influence of horizontal gradients on retrieved profiles from ATOMS occultation measurements: a promising approach for data assimilation, *Proc. Book, 1st Int'l Workshop on Occultations for Probing Atmosphere and Climate (OPAC-1)*, Sept. 2002, Graz, Austria, Springer Verlag.
- WegCenter/UniGraz (2006), Kirchengast, G., and M. Schwärz, Scientific Applications of Galileo K-band Links, *GADEM Project Tech. Note GAD-TN-002-UG*, 16 pp., Wegener Center, Univ. of Graz, Graz, Austria.



## Appendix A:

### A.1. Galileo Constellation Two Line Element (TLE) Files

```
Gal11
1 99911U          09182.50000000 -.00000166  00000-0 -12057+4 0 00000
2 99911 056.0190 000.0885 0002090 270.0283 090.0269 01.70476306000017
Gal12
1 99912U          09182.50000000 -.00000090  00000-0 -65450+3 0 00001
2 99912 056.0190 000.0885 0002089 269.9537 130.1016 01.70476209000013
Gal13
1 99913U          09182.50000000 .00000089  00000-0  64767+3 0 00008
2 99913 056.0190 000.0885 0002092 269.9853 170.0702 01.70476035000011
Gal14
1 99914U          09182.50000000 .00000073  00000-0  52838+3 0 00008
2 99914 056.0191 000.0885 0002090 270.0326 210.0228 01.70476076000012
Gal15
1 99915U          09182.50000000 -.00000117  00000-0 -84848+3 0 00006
2 99915 056.0190 000.0885 0002089 269.9407 250.1146 01.70476268000014
Gal16
1 99916U          09182.50000000 -.00000171  00000-0 -12377+4 0 00006
2 99916 056.0190 000.0885 0002092 269.9619 290.0934 01.70476298000015
Gal17
1 99917U          09182.50000000 -.00000001  00000-0 -10474+2 0 00003
2 99917 056.0190 000.0885 0002089 270.0111 330.0443 01.70476118000013
Gal18
1 99918U          09182.50000000 .00000112  00000-0  81444+3 0 00001
2 99918 056.0190 000.0885 0002089 269.9309 010.1246 01.70476023000012
Gal19
1 99919U          09182.50000000 -.00000014  00000-0 -98310+2 0 00004
2 99919 056.0191 000.0885 0002092 269.9669 050.0884 01.70476166000016
Gal21
1 99921U          09182.50000000 -.00000099  00000-0 -71423+3 0 00007
2 99921 055.9409 120.1473 0002093 269.9866 103.2527 01.70473965000015
Gal22
1 99922U          09182.50000000 .00000045  00000-0  32935+3 0 00002
2 99922 055.9409 120.1473 0002096 269.9044 143.3350 01.70473806000010
Gal23
1 99923U          09182.50000000 .00000187  00000-0  13569+4 0 00003
2 99923 055.9409 120.1472 0002098 269.9818 183.2578 01.70473680000016
Gal24
1 99924U          09182.50000000 .00000092  00000-0  66621+3 0 00005
2 99924 055.9409 120.1472 0002096 270.0004 223.2390 01.70473796000010
Gal25
1 99925U          09182.50000000 -.00000084  00000-0 -61207+3 0 00004
2 99925 055.9409 120.1472 0002097 269.9537 263.2856 01.70473964000018
Gal26
1 99926U          09182.50000000 -.00000052  00000-0 -37422+3 0 00002
2 99926 055.9409 120.1473 0002098 270.0436 303.1958 01.70473908000017
Gal27
1 99927U          09182.50000000 .00000135  00000-0  97953+3 0 00008
2 99927 055.9409 120.1472 0002094 270.0464 343.1931 01.70473721000012
Gal28
1 99928U          09182.50000000 .00000167  00000-0  12131+4 0 00000
2 99928 055.9409 120.1472 0002094 269.9621 023.2775 01.70473712000017
```

```

Gal29
1 99929U      09182.50000000 -.00000007  00000-0 -50710+2 0 00009
2 99929 055.9409 120.1472 0002095 270.0101 063.2293 01.70473894000015
Gal31
1 99931U      09182.50000000 -.00000050  00000-0 -36743+3 0 00001
2 99931 056.0431 240.1305 0002096 270.0350 116.6537 01.70476026000014
Gal32
1 99932U      09182.50000000 .00000134  00000-0  97089+3 0 00003
2 99932 056.0431 240.1305 0002099 270.0039 156.6849 01.70475837000011
Gal33
1 99933U      09182.50000000 .00000208  00000-0  15094+4 0 00003
2 99933 056.0431 240.1305 0002099 270.0759 196.6130 01.70475785000010
Gal34
1 99934U      09182.50000000 .00000051  00000-0  36644+3 0 00003
2 99934 056.0431 240.1305 0002096 270.0108 236.6779 01.70475955000019
Gal35
1 99935U      09182.50000000 -.00000079  00000-0 -57351+3 0 00004
2 99935 056.0431 240.1305 0002099 269.9750 276.7136 01.70476068000011
Gal36
1 99936U      09182.50000000 .00000031  00000-0  22646+3 0 00000
2 99936 056.0431 240.1305 0002099 270.0556 316.6331 01.70475938000015
Gal37
1 99937U      09182.50000000 .00000196  00000-0  14215+4 0 00007
2 99937 056.0431 240.1305 0002097 270.0096 356.6792 01.70475784000017
Gal38
1 99938U      09182.50000000 .00000141  00000-0  10236+4 0 00007
2 99938 056.0431 240.1305 0002099 269.9938 036.6950 01.70475862000010
Gal39
1 99939U      09182.50000000 -.00000043  00000-0 -31329+3 0 00006
2 99939 056.0431 240.1305 0002099 270.0848 076.6038 01.70476043000017

```

## A.2. METOP Constellation Two Line Element (TLE) Files

```

METOP-1
1      1  04001USR  9182.50000000 .00000000  00000-0  00000-0 0 0010
2      1  98.7003  62.80000 0010000  90.0000  6.0000 14.19847837  0

```

## A.3. Ground Station Properties

Id	Station name	h [m]	phi[deg]	lambda[deg]	betalim [deg]
1	Malindi (Kenya)	22.7	-3.00000	40.19000	15.000
2	Maspalomas (Canaries)	197.3	27.76000	-15.63000	15.000
3	Kiruna (Sweden)	391.1	67.86000	20.97000	15.000
4	Rio Grande (Argentina)	32.0	-53.79000	-67.75000	15.000
5	Yogyakarta (Indonesia)	2.0	-7.50000	107.25000	15.000
6	Mizusawa (Japan)	75.6	39.14000	141.13000	15.000
7	Dunedin (New Zealand)	26.2	-45.68000	170.51000	15.000
8	Tahiti (Tahiti)	98.0	-17.57690	-149.60630	15.000
9	Albert Head (Canada)	32.0	48.38980	-123.42740	15.000
10	Guayaquil (Equador)	68.6	-2.19000	-79.88100	15.000

## A.4. Mission Analysis/Planning input (example)

```
[*Project-Id and Task-Id*]
Input File Version           = EGOPsv5.2
Creation Date & Time         = 2006 Jun 12 17:18:35
Project-Id                   = GADEMPperfAnal
Task-Type                    = MAnPl
Task-Id                      = GADEM2Freq-lowLat

[*Data Type Selection*]
Data Type                    = LEO-LEO Occultation Data

[*UT Range*]
Start_Time                   = 090701.000000 [yyymmdd.hhmmss]
Simul_Time_Range             = 0240000      [hhmmss]

[*Height Levels*]
Hlo1 Hhi1 HStep1 dh1         = 1.0 13.0 4.0 0.20 [km]
Hlo2 Hhi2 HStep2 dh2         = 20.0 80.0 20.0 0.20 [km]

[*Geographic Area of Interest*]
GeogrAreaChoice              = Regional
LaMin LaMax LoMin LoMax      = -20.0 20.0 -180.0 180.0 [deg]

[*Earth Figure Model*]
EarthFigModelChoice          = Ellip.WGS84

[*Tx-to-Rx Ray Treatment*]
RayTreatmentChoice           = Bended Rays (Exp. Atmos.)

[*Tx System Specifications*]
Tx SatSystemChoice           = GAL
Tx OrbitModelChoice          = SGP Orbits (Impr. Kepler)
Tx1 OrbitElemFilename        = Tx-GAL-2009182.tle
Tx1 SignalPropFilename       = Tx-GAL-KBand2.spd

[*Tx Antenna Specifications*]
Tx -V AntennaChoice          = Used
Tx -V BoresightElevation     = 77.0 [deg]
Tx -V BoresightAzimuth       = 180.0 [deg]
Tx -V FOVChoice              = Ell_Cartes
Tx -V TPBW Vertical          = 90.0 [deg]
Tx -V TPBW Horizontal        = 120.0 [deg]
Tx +V AntennaChoice          = Used
Tx +V BoresightElevation     = 77.0 [deg]
Tx +V BoresightAzimuth       = 0.0 [deg]
Tx +V FOVChoice              = Ell_Cartes
Tx +V TPBW Vertical          = 90.0 [deg]
Tx +V TPBW Horizontal        = 120.0 [deg]

[*Rx System Specifications*]
Rx SatSystemChoice           = MetOp1
Rx OrbitModelChoice          = SGP Orbits (Impr. Kepler)
Rx OrbitElemFilename         = Rx-MetOp1-2009182.tle

[*Rx Antenna Specifications*]
Rx -V AntennaChoice          = Used
Rx -V BoresightElevation     = 27.0 [deg]
Rx -V BoresightAzimuth       = 180.0 [deg]
```

```
Rx -V FOVChoice           = Ell_Cartes
Rx -V TPBW Vertical        = 30.0 [deg]
Rx -V TPBW Horizontal      = 100.0 [deg]
Rx +V AntennaChoice        = Used
Rx +V BoresightElevation   = 27.0 [deg]
Rx +V BoresightAzimuth     = 0.0 [deg]
Rx +V FOVChoice            = Ell_Cartes
Rx +V TPBW Vertical        = 30.0 [deg]
Rx +V TPBW Horizontal      = 100.0 [deg]
Rx ZenithAntElevationLim   = 10.0 [deg]

[*Visibility Infos on Differencing*]
DiffVisInfChoice           = No_Diff_Vis_info
TrackVisInfChoice          = No_Track_Vis_info

[* EOF *]
```

## A.5. Forward Modeling input (example)

```
[*Project-Id and Task-Id*]
Input File Version         = EGOPsv5.2
Creation Date & Time       = 2006 Jun 14 10:53:07
Project-Id                 = GADEMPerfAnal
Task-Type                  = FoMod
Task-Id                    = F-GADEM2Freq-lowLat

[*Occ. Event Simulation Type/Specifications*]
OccEventSimulType          = Sample of Events/Realistic Geometry
ReferenceMANPl/Task-Id     = GADEM2Freq-lowLat
OccNoRange                 = 59 67 1
OccEv.HeightRange          = 1.0 80.0 [km]

[*Atmospheric Models Choice/Specifications*]
AtmModelChoice             = GCM 3D Atmosphere (GCM3DAtm)
GRIB Data FilePath         =
/usr/people/phyk/schwaerm/work/data/ecmwf/T511/
GRIB Data FileName         = ecmwf20090701121.grb
AtmModelStructureChoice    = Atmos. Model Structure as is
HumidityChoice             = Humidity included (moist air)
CloudsandRainChoice        = GCM 3D Clouds LWC+IWC
AtmDistModelChoice         = No Atmos. Disturbance
AtmTurbModelChoice         = IEP Turbulence/Scintillations
TurbScintModelType         = Standard Model
TurbReferenceHeight        = 0.0 [km]
Turb_Cn2_RefHeight         = 1.30E-15 [m-(2/3)]
TurbVerticalStructure       = Exponential
TurbVerticalScale          = 2.0 [km]
TurbHorizontalExtend       = 200.0 [km]

[*Ionospheric Models Choice/Specifications*]
IonModelChoice             = No Ionosphere

[*Signal Propagation Simulator Specifications*]
PropSimulatorType          = Full-3D Ray Tracer
PropSimulatorAccuracy       = < ~1 mm
Extended Data Output        = Dopp-Tran-Bend-pLC1 Data

[*Earth Figure Model*]
EarthFigModelChoice        = Ellip.WGS84
```

```

[*Tx-to-Rx Ray Treatment*]
RayTreatmentChoice                = Bended Rays (Exp. Atmos.)

[*Tx System Specifications*]
Tx SatSystemChoice                = GAL
Tx OrbitModelChoice               = SGP Orbits (Impr. Kepler)
Tx1 OrbitElemFilename             = Tx-GAL-2009182.tle
Tx1 SignalPropFilename            = Tx-GAL-KBand2.spd

[*Tx Antenna Specifications*]
Tx -V AntennaChoice               = Used
Tx -V BoresightElevation           = 77.0 [deg]
Tx -V BoresightAzimuth            = 180.0 [deg]
Tx -V FOVChoice                   = Ell_Cartes
Tx -V TPBW Vertical                = 90.0 [deg]
Tx -V TPBW Horizontal             = 120.0 [deg]
Tx +V AntennaChoice               = Used
Tx +V BoresightElevation           = 77.0 [deg]
Tx +V BoresightAzimuth            = 0.0 [deg]
Tx +V FOVChoice                   = Ell_Cartes
Tx +V TPBW Vertical                = 90.0 [deg]
Tx +V TPBW Horizontal             = 120.0 [deg]

[*Rx System Specifications*]
Rx SatSystemChoice                = MetOp1
Rx OrbitModelChoice               = SGP Orbits (Impr. Kepler)
Rx OrbitElemFilename              = Rx-MetOp1-2009182.tle
Rx Sampling Rate                  = 10 [Hz]

[*Rx Antenna Specifications*]
Rx -V AntennaChoice               = Used
Rx -V BoresightElevation           = 27.0 [deg]
Rx -V BoresightAzimuth            = 180.0 [deg]
Rx -V FOVChoice                   = Ell_Cartes
Rx -V TPBW Vertical                = 30.0 [deg]
Rx -V TPBW Horizontal             = 100.0 [deg]
Rx +V AntennaChoice               = Used
Rx +V BoresightElevation           = 27.0 [deg]
Rx +V BoresightAzimuth            = 0.0 [deg]
Rx +V FOVChoice                   = Ell_Cartes
Rx +V TPBW Vertical                = 30.0 [deg]
Rx +V TPBW Horizontal             = 100.0 [deg]

[* EOF *]

```

## A.6. Observation System Modeling input (example)

```

[*Project-Id and Task-Id*]
Input File Version                = EGOPsv5.2
Creation Date & Time              = 2006 Jul 12 17:54:31
Project-Id                        = GADEMPerfAnal
Task-Type                         = OSMod
Task-Id                           = O-GADEM2Freq-11

[*Occ. Event Simulation Type/Specifications*]
OccEventSimulType                 = Sample of Events/Realistic Geometry
OccEv.HeightRange                 = 1.0 80.0 [km]
ReferenceFoMod/Task-Id            = F-GADEM2Freq-lowLat

```

# Performance Analysis for Atmospheric Data from Galileo K-band Links

GADEM – Galileo Atmospheric Data Enhancement Mission

---

OccNoRange = 1 67 1

[\*POD Error Modeling/Specifications\*]

PODErrorModelChoice = No POD Errors

[\*Tx-Rx System Simulator Specifications\*]

TxRx SysSimulatorType = Parameterized Receiving System

Simulator

Extended Data Output = C/N0 and Antenna Data

[\*Tx System Specifications\*]

Tx SatSystemChoice = GAL

Tx OrbitModelChoice = SGP Orbits (Impr. Kepler)

Tx1 OrbitElemFilename = Tx-GAL-2009182.tle

Tx1 SignalPropFilename = Tx-GAL-KBand2.spd

[\*Tx Antenna Specifications\*]

Tx -V AntennaChoice = Used

Tx -V BoresightElevation = 77.0 [deg]

Tx -V BoresightAzimuth = 180.0 [deg]

Tx -V FOVChoice = Ell\_Cartes

Tx -V HPBW Vertical = 90.0 [deg]

Tx -V HPBW Horizontal = 120.0 [deg]

Tx -V AntGain/Boresight (at 1 GHz) = 13.0 [dB]

Tx -V BoresightTracking = n/a

Tx +V AntennaChoice = Used

Tx +V BoresightElevation = 77.0 [deg]

Tx +V BoresightAzimuth = 0.0 [deg]

Tx +V FOVChoice = Ell\_Cartes

Tx +V HPBW Vertical = 90.0 [deg]

Tx +V HPBW Horizontal = 120.0 [deg]

Tx +V AntGain/Boresight (at 1 GHz) = 13.0 [dB]

Tx +V BoresightTracking = n/a

[\*Tx Performance Modeling\*]

TxPerformModelChoice = No Transmitter Perf. Model

[\*Rx System Specifications\*]

Rx SatSystemChoice = MetOp1

Rx OrbitModelChoice = SGP Orbits (Impr. Kepler)

Rx OrbitElemFilename = Rx-MetOp1-2009182.tle

Rx Sampling Rate = 10 [Hz]

[\*Rx Antenna Specifications\*]

Rx -V AntennaChoice = Used

Rx -V BoresightElevation = 27.0 [deg]

Rx -V BoresightAzimuth = 180.0 [deg]

Rx -V FOVChoice = Ell\_Cartes

Rx -V HPBW Vertical = 10.0 [deg]

Rx -V HPBW Horizontal = 30.0 [deg]

Rx -V AntGain/Boresight (at 1 GHz) = 14.8 [dB]

Rx -V BoresightTracking = Yes

Rx +V AntennaChoice = Used

Rx +V BoresightElevation = 27.0 [deg]

Rx +V BoresightAzimuth = 0.0 [deg]

Rx +V FOVChoice = Ell\_Cartes

Rx +V HPBW Vertical = 10.0 [deg]

Rx +V HPBW Horizontal = 30.0 [deg]

Rx +V AntGain/Boresight (at 1 GHz) = 14.8 [dB]

Rx +V BoresightTracking = Yes

[\*Rx Performance Modeling\*]

RxThermNoiseModelChoice = LEO-LEO Thermal Noise Model

```

ChannelsC/N0Adjustment          =   -0.04   -0.09    0.00 [dBHz]
AntennaNoiseTemp (at 10 GHz)    =   80.0 [K]
ReceiverNoiseTemp (at 10 GHz)   =  160.0 [K]
Rx1/fNoiseModelChoice           = No 1/f Amplitude Noise
RxPolyAmplDriftModel            = Polynomial Ampl. Drift Model
DriftApplicationType            = Apply drifts randomly (as rms)
PolyReferenceHeight             =   25.0 [km]
LinearDriftSlope                =    0.060 [dB/min]
QuadrDriftCurvature            =    0.0000 [dB/min2]
3rdOrderDriftCurvChange        =    0.00000 [dB/min3]
RxSinAmplDriftModel            = No Sinusoidal Ampl. Drifts

[*Local Multipath Modeling*]
LocalMultipModelChoice          = No Local Multipath

[*Differencing Treatment/Clocks Modeling*]
DiffTreatClocksChoice          = Perfect Clocks (No Differencing)

[*Atmospheric Models Choice/Specifications*]
AtmModelChoice                 = GCM 3D Atmosphere (GCM3DATm)
GRIB Data FilePath             = /home/mas/work/data/ecmwf/T511/
GRIB Data FileName             = ecmwf20090701121.grb
AtmModelStructureChoice        = Atmos. Model Structure as is
HumidityChoice                 = Humidity included (moist air)
CloudsandRainChoice            = GCM 3D Clouds LWC+IWC
AtmDistModelChoice             = No Atmos. Disturbance
AtmTurbModelChoice             = IEP Turbulence/Scintillations
TurbScintModelType             = Standard
TurbReferenceHeight            =    0.0 [km]
Turb_Cn2_RefHeight            = 1.30E-15 [m-(2/3)]
TurbVerticalStructure          = Exponential
TurbVerticalScale              =    2.0 [km]
TurbHorizontalExtend           =   200.0 [km]

[*Ionospheric Models Choice/Specifications*]
IonModelChoice                 = No Ionosphere

[*Earth Figure Model*]
EarthFigModelChoice            = Ellip.WGS84

[* EOF *]

```

## A.7. Inversion/Retrieval input (example)

```

[*Project-Id and Task-Id*]
Input File Version              = EGOPsv5.2
Creation Date & Time            = 2006 Jul 12 18:24:12
Project-Id                     = GADEMPerfAnal
Task-Type                      = InRet
Task-Id                        = I-GADEM2Freq-11

[*Occ. Event Type/Specifications*]
OccDataType                    = SimData
OccEventType                   = Sample of Events/Realistic Geometry
OccNoRange                    =    1    67    1
OccEv.HeightRange              =    1.0  80.0 [km]
ReferenceOSMod/Task-Id         = O-GADEM2Freq-11

```

# Performance Analysis for Atmospheric Data from Galileo K-band Links

GADEM – Galileo Atmospheric Data Enhancement Mission

---

```
[*Tx System Specifications*]
Tx SatSystemChoice           = GAL
Tx1 SignalPropFilename      = Tx-GAL-KBand2.spd

[*Bending Angle and Transmission Retrieval Specifications*]
BendAngleRetToolChoice       = Advanced Geom.Optics Bend.Angle
Retrieval
IonoCorrectionType           = Phase Correction
StatOptimizationType         = Opt. using BenA Search (MSIS90)
TransmRetToolChoice          = Standard Channel Transmission
Retrieval
I/I0 RefHeightperChannel     = 25.0 25.0 25.0 [km]
I0Value AvHeightInterval     = 4.0 [km]

[*Refractivity Profiles Retrieval Specifications*]
RefProfRetToolChoice         = Abel Transform Refr. + Absorption
Coeff. Profiles
TransmissionProcessingType    = Differential Transmissions

[*Atmospheric Profiles Retrieval Specifications*]
AtmProfRetToolChoice         = Refr. + AbsCoeff. Based Atmos.
Profiles
RefrAbsCoeffInvRetType       = T,q,e,p,rho,w by Opt.Inverse
Estimation
RefrErrorModelChoice         = 1/z (<zRef) + exp(z) (>zRef) Errors
RefrRMSError_zRef            = 0.10 [%] (zRef: 15 km)
AbsCoeffErrorModelChoice     = ScaleFactor*RMS(z0)*W(z) SNR-based
Errors
AbsCoeffRMSErrScaleFactor    = 0.50 [1] (ScaleFactor)
AtmProfRetrievalMode         = p+T+q+w (cloudy air) Retrieval
AtmBackgroundMode           = Best-fit T at z < zBestfitTop
AtmModelfBestFit             = GCM 3D Atmosphere (GCM3DAtm)...
GRIB Data FilePath           = /home/mas/work/data/ecmwf/T511/
GRIB Data FileName           = ec24h20090701121.grb

[*Atmospheric Models Choice/Specifications*]
AtmModelChoice               = GCM 3D Atmosphere (GCM3DAtm)
GRIB Data FilePath           = /home/mas/work/data/ecmwf/T511/
GRIB Data FileName           = ecmwf20090701121.grb
AtmModelStructureChoice      = Atmos. Model Structure as is
HumidityChoice               = Humidity included (moist air)
CloudsandRainChoice          = GCM 3D Clouds LWC+IWC
AtmDistModelChoice           = No Atmos. Disturbance
AtmTurbModelChoice           = IEP Turbulence/Scintillations
TurbScintModelType           = Standard
TurbReferenceHeight          = 0.0 [km]
Turb_Cn2_RefHeight           = 1.30E-15 [m-(2/3)]
TurbVerticalStructure         = Exponential
TurbVerticalScale            = 2.0 [km]
TurbHorizontalExtend         = 200.0 [km]

[*Ionospheric Models Choice/Specifications*]
IonModelChoice               = No Ionosphere

[*Earth Figure Model*]
EarthFigModelChoice          = Ellip.WGS84

[* EOF *]
```

– end of document –